UNIVERSIDADE FEDERAL DE MINAS GERAIS
School of Engineering
Graduate Program in Electrical Engineering

Alice Helena Teixeira Silva

SiC component thermal modeling and junction temperature measurement in inverter operation

Belo Horizonte

2024

Alice Helena Teixeira Silva

SiC component thermal modeling and junction temperature measurement in inverter operation

Final thesis presented to the Graduate Program in Electrical Engineering of the Universidade Federal de Minas Gerais in partial fulfillment of the requirements for the degree of Master in Electrical Engineering.

Advisor: Prof. Dr. Lenin Martins Ferreira Morais
Co-advisor: Dr. Bernardo Cougo França

Belo Horizonte
2024

S586s

Silva, Alice Helena Teixeira.
SiC component thermal modeling and junction temperature measurement in inverter operation [recurso eletrônico] / Alice Helena Teixeira Silva. – 2024.
1 recurso online (87 f. : il., color.) : pdf.

Orientador: Lenin Martins Ferreira Morais.
Coorientador: Bernardo Cougo França.

Dissertação (mestrado) – Universidade Federal de Minas Gerais, Escola de Engenharia.

Bibliografia: f. 81-87.

1. Engenharia elétrica – Teses. 2. Modelagem de processos – Teses. 3. Impedância (Eletricidade) – Teses. 4. Medição de temperatura – Teses. 5. Transistores de potência – Teses. I. Morais, Lenin Martins Ferreira. II. França, Bernardo Cougo. III. Universidade Federal de Minas Gerais. Escola de Engenharia. IV. Título.

CDU: 621.3(043)

Ficha catalográfica elaborada pelo Bibliotecário Marcio A. A. Gomes CRB/6 2812
Biblioteca Prof. Mário Werneck, Escola de Engenharia da UFMG

UNIVERSIDADE FEDERAL DE MINAS GERAIS
UNIVERSIDADE FEDERAL DE MINAS GERAIS
ENGENHARIA - COLEGIADO DE PÓS-GRADUAÇÃO EM ENGENHARIA ELÉTRICA

"Sic Component Thermal Modeling And Junction Temperature Measurement In Inverter Operation"

Alice Helena Teixeira Silva

Dissertação de Mestrado submetida à Banca Examinadora designada pelo Colegiado do Programa de Pós-Graduação em Engenharia Elétrica da Escola de Engenharia da Universidade Federal de Minas Gerais, como requisito para obtenção do grau de Mestre em Engenharia Elétrica.

Aprovada em 26 de agosto de 2024.

Por:

Prof. Dr. Lenin Martins Ferreira Morais
DELT (UFMG) - Orientador

Dr. Bernardo Cogo França
IRT Saint Exupéry - França - Coorientador

Prof. Dr. Thiago Ribeiro de Oliveira
DELT (UFMG)

Profa. Dra. Renata Oliveira de Sousa
(UTFPR)

Documento assinado eletronicamente por **Lenin Martins Ferreira Morais**, **Professor do Magistério Superior**, em 26/08/2024, às 12:13, conforme horário oficial de Brasília, com fundamento no art. 5º do Decreto nº 10.543, de 13 de novembro de 2020.

Documento assinado eletronicamente por **Thiago Ribeiro de Oliveira**, **Professor do Magistério Superior**, em 26/08/2024, às 12:51, conforme horário oficial de Brasília, com fundamento no art. 5º do Decreto nº 10.543, de 13 de novembro de 2020.

Documento assinado eletronicamente por **Renata Oliveira de Sousa**, **Usuária Externa**, em 26/08/2024, às 18:17, conforme horário oficial de Brasília, com fundamento no art. 5º do Decreto nº 10.543, de 13 de novembro de 2020.

Documento assinado eletronicamente por **Bernardo Cogo França**, **Usuário Externo**, em 28/08/2024, às 09:04, conforme horário oficial de Brasília, com fundamento no art. 5º do Decreto nº 10.543, de 13 de novembro de 2020.

A autenticidade deste documento pode ser conferida no site https://sei.ufmg.br/sei/controlador_externo.php?acao=documento_conferir&id_orgao_acesso_externo=0, informando o código verificador **3488471** e o código CRC **1AAA9483**.

Referência: Processo nº 23072.247502/2024-30 SEI nº 3488471

I dedicate this work to my family.

Acknowledgments

I would first like to thank my parents, Cláudio and Kátia, for being my role models and for all their support and encouragement throughout my academic journey. They have encouraged me from a young age, not only to study but also to read, play sports, and learn musical instruments—everything that has shaped who I am today. Without their upbringing, I would not have believed I was capable of completing this work. I am also grateful to my brother, Arthur, for being my lifelong companion.

I extend my thanks to my advisor, Professor Lenin Morais, for his trust, support, patience, and guidance throughout this work. Our relationship dates back to my undergraduate studies, where I had the pleasure of being his student and was also guided by him during my undergraduate thesis. I am deeply thankful for all his teachings.

I also thank my co-advisor, Dr. Bernardo Cougo, for the invitation to work alongside him at IRT Saint Exupery. Those six months were a period of immense learning.

Additionally, I would like to express my gratitude to all the professors I had during my undergraduate and master's studies who contributed to my education.

I am extremely grateful to everyone who supported and assisted me, directly or indirectly, in the completion of this work.

This work was carried out with the support of the Coordination for the Improvement of Higher Education Personnel - Brazil (CAPES) through the Academic Excellence Program (PROEX).

"On ne voit bien qu'avec le coeur. L'essentiel est invisible pour les yeux."
Antoine de Saint-Exupéry

Resumo

A medição precisa da temperatura do ciclo térmico é fundamental para estimar a vida útil dos módulos de potência, especialmente aqueles feitos com transistores SiC MOSFET com capacitância térmica muito baixa. Este trabalho mostra um método preciso para estimar a temperatura dinâmica dos componentes SiC que compõem um módulo de potência usado em inversores trifásicos. Esse método baseia-se no uso de uma câmera térmica rápida para medir com precisão a impedância térmica de cada chip. Os resultados das medições da câmera térmica são validados por comparação com as medições clássicas de resistência no estado de condução para estimar a temperatura de junção. O modelo de impedância térmica é então acoplado ao cálculo preciso de perda para para prever a temperatura dinâmica do MOSFET de SiC durante a operação em um inversor trifásico. As medições da variação de temperatura de componentes SiC de um módulo de potência operando como inversor trifásico de 540V/7,5kW para aplicações aeronáuticas mostram a precisão do modelo desenvolvido para a estimativa da temperatura dinâmica da junção.

Palavras-chave: Ciclo térmico; SiC MOSFET; Câmera térmica; Impedância térmica; Perdas de semicondutores.

Abstract

Precise thermal cycle temperature measurement is fundamental to estimate lifetime of power modules, especially those made with SiC MOSFET transistors having very low thermal capacitance. This work shows a precise method to estimate dynamic temperature of SiC components composing a power module used in three-phase inverters. This method is based on the use of a fast thermal camera to precisely measure thermal impedance of each die. Results of thermal camera measurements are validated by comparison with classical on-state resistance measurements to estimate junction temperature. Thermal impedance model is then coupled with precise loss calculation in order to predict dynamic SiC die temperature during operation in a three-phase inverter. Measurements of the temperature variation of SiC MOSFET dies conducting typical currents of a 540V/7.5kW three-phase inverter for aeronautical applications show the accuracy of the developed model for dynamic junction temperature estimation.

Keywords: Thermal cycle; SiC MOSFET; Thermal camera; Thermal impedance; Semiconductor losses.

List of Figures

Figure 1 – Number of cycles to failure versus temperature variation of a MOSFET die in a power module for automotive applications. 19
Figure 2 – Cross section of a typical SiC power MOSFET structure. 23
Figure 3 – Example of inductive electric circuit. 25
Figure 4 – Bond wire lift-off and heel cracking in a SiC chip. 26
Figure 5 – X-Ray images of die attach layer: a) pre-cycling and b) post-cycling. . . 26
Figure 6 – Zth characteristics of silicon IGBT and SiC MOSFET. 27
Figure 7 – Power Cycling test results and lifetime models for SiC power Module. . 28
Figure 8 – Schematic diagram of the proposed setup: Red quantities are measured online. 29
Figure 9 – Schematic circuit for quasi-threshold voltage measurement. 30
Figure 10 – Schematic circuit for gate current peak detection. 31
Figure 11 – Schematic circuit for measurement of peak voltage and current across L'_{SS}. 32
Figure 12 – Micro-Raman set-up (schematically). 33
Figure 13 – Schematic diagram of the thermal microscopy imaging device based on thermoreflectance thermography. 34
Figure 14 – Die temperature measurement using a thermocouple based on a representative case of TO-220. 37
Figure 15 – Flir thermal camera model x6900sc. 40
Figure 16 – Thermal camera software - Research IR. 41
Figure 17 – Single SiC die: (a) close-up picture, (b) thermal image showcasing different ROIs. 42
Figure 18 – Die temperatures measured by the camera for different ROIs. 43
Figure 19 – SiC power module with 3 switching cells using 1200V/80mΩ SiC MOSFETs. 44
Figure 20 – Electrical circuit for constant current imposition (and quasi-constant losses) on SiC dies for thermal impedance characterization. 44
Figure 21 – DC power suply current 45
Figure 22 – Experimental setup for determining the thermal impedance of SiC dies. 45
Figure 23 – Waveforms of currents and voltages of the components during the tests for determining thermal impedance. 46
Figure 24 – DUT current with detail to the 500μs necessary to be stable at the DUT. 47
Figure 25 – Experimental results for current of 15A at 25°C. 48

Figure 26 – Calculated R_{DSon} for a current of 15A with a pulse duration of 1ms for 25°C, 75°C, 100°C. 49
Figure 27 – R_{DSon} versus T_j characteristic for different currents, given by the datasheet (dotted lines) and that measured with a thermal camera (solid lines), of the 1200V/80 mΩ SiC MOSFET die. 49
Figure 28 – Experimental results showing the time variation of the DUT temperature measured by the thermal camera, superimposed on the current, voltage and power curves measured on the same DUT, for an applied current of 25A. 50
Figure 29 – Electrical circuit for constant current imposition (and quasi-constant losses) on SiC dies for thermal impedance characterization. 51
Figure 30 – Excel spreadsheet to calculate the thermal model. 51
Figure 31 – Excel spreadsheet to calculate the thermal model. 52
Figure 32 – Excel solver used for finding the best solution with minimum error. . . 52
Figure 33 – DUT (a) losses and (b) temperature variation for positive currents of 15A, 20A and 25A. 53
Figure 34 – Instantaneous thermal impedance for 15A, 20A and 25A and applied power losses. 54
Figure 35 – Instantaneous power for current applied in positive and negative directions to the DUT, and at different V_{gs}. 54
Figure 36 – Instantaneous thermal impedance for current applied in positive and negative directions to the DUT, and at different V_{gs}. 55
Figure 37 – Current's path in the MOSFET when the current is negative with high V_{gs}. 56
Figure 38 – Current's path in the MOSFET when the current is positive with high V_{gs}. 56
Figure 39 – Current's path in the MOSFET when the current is negative with low or zero V_{gs}. 57
Figure 40 – Measurement of instantaneous temperature of the SiC die (averaged over the die surface) and of the 3 neighbouring dies, for a current of 25A (positive) applied to the DUT only. 58
Figure 41 – Sinusoidal current (I_{ds}, 10A/div) and voltage (I_{ds}, 10V/div) measured on the SiC die and instantaneous losses (10W/div) calculated in this die (with imposed current of 17.6Arms at 50Hz). 59
Figure 42 – Temperature and instantaneous losses measured in the SiC die using, respectively, a high-speed thermal camera and an oscilloscope. 60
Figure 43 – Calculated thermal impedance of SiC die for: (a) different current and (b) different frequencies of current applied to the die. 60
Figure 44 – Electrical circuit of a three-phase inverter. 63

Figure 45 – Set up for temperature measurement in a three-phase inverter. 63
Figure 46 – Measured current and voltage of 540V/10kW three-phase inverter, having total losses of only 212W. 64
Figure 47 – Thermal image of SiC power module at V_{DC} = 540V, f_{fund} = 50Hz, f_{sw} = 50kHz, M_i = 0.9 and I_{out} = 21.11Arms. 64
Figure 48 – Temperature measurement of SiC dies of the low side in three different legs of the inverter with f_{fund} = 50Hz, f_{sw} = 50kHz, M_i = 0.85, I_{rms} = 14.73A and SPWM method. 65
Figure 49 – Temperature measurement of different points in the same SiC die with f_{fund} = 50Hz, f_{sw} = 50kHz, M_i = 0.9, I_{rms} = 21.11A and SPWM method. 65
Figure 50 – Junction temperature variation for load variation. 67
Figure 51 – Semiconductor losses versus modulation index. 68
Figure 52 – Junction temperature variation for M_i variation. 68
Figure 53 – Modulation waveforms of the modern PWM methods (M_i = 0,7). . . . 69
Figure 54 – Generating the GDPWM zero-sequence signal with the ψ variable. . . . 70
Figure 55 – Measured temperature for different PWM methods. 71
Figure 56 – Measured temperature for fundamental frequencies of 10, 20, 30, 50, 100 and 200Hz (normalized for the 10Hz period). 72
Figure 57 – Measured temperature for switching frequencies of 20kHz, 30kHz and 50kHz. 73
Figure 58 – Instantaneous (a) conduction,(b) switching and (c) total losses in SiC dies in a switching leg of a three-phase with f_{fund} = 50Hz, f_{sw} = 50kHz, M_i = 0.9 and SPWM method. 75
Figure 59 – Junction temperature in SiC die: measured and calculated using the developed thermal model (f_{fund} = 50Hz, f_{sw} = 50kHz, M_i = 0.9 and SPWM method). 76
Figure 60 – Instantaneous values of (a) conduction,(b) switching and (c) total losses in a three-phase inverter with f_{fund} = 50Hz, f_{sw} = 50kHz and M_i = 0.357 and SPWM method. 76
Figure 61 – Junction temperature in SiC die: measured and calculated by thermal model using (a) average temperature and (b) single point temperature (f_{fund} = 50Hz, f_{sw} = 50kHz and M_i = 0.357 and SPWM method). . . 77
Figure 62 – Junction temperature in SiC die: measured and calculated by thermal model using single point method (f_{fund} = 50Hz, f_{sw} = 50kHz and M_i = 0.357, I = 21.11Arms and SPWM method). 77

List of Tables

Table 1 – Advantages and disadvantages of generic methods for measuring temperature of semiconductor devices. 38
Table 2 – List of instruments used in the set-up and their features. 46
Table 3 – Thermal resistances and capacitances values of the SiC die in a power module, for different current conduction modes. 57
Table 4 – Parameters for inverter nominal operation. 66
Table 5 – Values of current, input power, output power and total losses for load variation (* Decrease in losses probably caused by a measurement error). 66
Table 6 – Values of input power, output power and total losses for modulation index variation (* A measurement error likely occurred, as the losses were expected to remain nearly constant). 68
Table 7 – Values of input power, output power and total losses for PWM method variation. 70
Table 8 – Values of current, input power, output power and total losses for fundamental frequency variation. 71
Table 9 – Values of current, input power, output power and total losses for switching frequency variation (* A higher than expected value, likely caused by a measurement device error). 72
Table 10 – Thermal resistances and capacitances values of the SiC die in a power module, calculated by using temperature measured in a single pixel on the top metallization of the SiC die. 75

List of Abbreviations and Acronyms

CCD	Charge-Coupled Device
CTE	Coefficient of Thermal Expansion
CPWM	Continuous Pulsed Width Modulation
DBC	Direct Bonded Copper
DPWM	Discontinuous Pulsed Width Modulation
DUT	Device Under Test
ESR	Equivalent Series Resistance
GaN	Gallium Nitride
IGBT	Insulated Gate Bipolar Transistor
IR	Infrared
LC	Liquid Crystals
LWIR	Long-Wave Infrared
MWIR	Medium-Wave Infrared
MOSFET	Metal Oxide Semiconductor Field Effect Transistor
NTC	Negative Temperature Coefficient
PCT	Power Cycling Test
PTC	Positive Temperature Coefficient
PWM	Pulsed Width Modulation
ROI	Region of Interest
SBD	Schottky Barrier Diode
Si	Silicon
SiC	Silicon Carbide
SiO_2	Silicon Dioxide

SLS	Strained Layer Superlattice
SMPS	Switch Mode Power Supply
SPWM	Sinusoidal Pulsed Width Modulation
SVPWM	Space Vector Pulsed Width Modulation
TSEP	Temperature Sensitive Electrical Parameters
WBG	Wide Band Gap
WFG	Waveform Generator

List os Symbols

dV/dt	rate of change of voltage over time
dI/dt	rate of change of current over time
f_{fund}	fundamental frequency
f_{sw}	switching frequency
I_{DS}	drain-source current
i_g	gate current
$I_{out,rms}$	inverter output current
M_i	modulation index
P_{in}	input power
P_{out}	output power
R_g	inverter gate driver resistance
R_{Gint}	internal gate resistance
R_{DSon}	on-state resistance
ΔT_j	temperature swing
T_j	junction temperature
t_{on}	power-on time
V_{br}	breakdown voltage
V_{th}	threshold voltage
V_{DC}	inverter direct current voltage
V_{ds}	drain-source voltage
V_{gs}	gate-source voltage
Zth	thermal impedance

Contents

Contents 17
1 Introduction 19
1.1 Objectives 20
1.1.1 General Objectives 20
1.1.2 Specific Objectives 20
1.2 Published Articles 21
1.3 Thesis structure 21
2 State of the Art 22
2.1 SiC reliability 22
2.1.1 Failure Mechanisms 22
2.1.1.1 Gate threshold voltage degradation 23
2.1.1.2 Body diode degradation 23
2.1.1.3 Degradation in gate leakage current 24
2.1.1.4 Avalanche events 24
2.1.1.5 Degradation under power cycling stress 25
2.1.2 Lifetime models 26
2.2 Temperature measurement methods 28
2.2.1 Electrical methods 28
2.2.1.1 On-State Voltage 29
2.2.1.2 Threshold Voltage 30
2.2.1.3 Internal Gate Resistance 30
2.2.1.4 Switching Rate of the Drain Current 31
2.2.2 Optical Methods 32
2.2.2.1 Luminescence 32
2.2.2.2 Raman 33
2.2.2.3 Thermoreflectance 34
2.2.2.4 Infrared 35
2.2.3 Physical contact methods 36
2.2.3.1 Thermographic Phosphors 36
2.2.3.2 Thermocouple 36
2.2.3.3 Liquid crystals 37
2.3 Chapter Overview 37
3 SiC Thermal Model 39
3.1 Thermal camera 39
3.1.1 Thermal analysis 42

3.2 Experimental setup for determining thermal impedance 43
3.3 Justifying the use of thermal cameras 47
3.4 Determining SiC die thermal model 50
3.4.1 Curve fitting 51
3.5 Experimental results for determining the thermal model 53
3.5.1 Variation of thermal impedance with losses 53
3.5.2 Variation of thermal impedance with current direction 54
3.6 Heat-coupling effects 57
3.7 Partial validation of thermal modules 58
3.8 Chapter overview 61
4 Temperature measurement in real three-phase inverter 62
4.1 Parameters Variation 66
4.1.1 Load Variation 66
4.1.2 Modulation Index Variation 67
4.1.3 PWM Method Variation 69
4.1.4 Fundamental frequency variation 71
4.1.5 Switching frequency Variation 72
4.2 Precise Loss Calculation in Three-Phase Converters 73
4.2.1 Conduction Losses 73
4.2.2 Switching Losses 74
4.3 Comparison with thermal model 74
4.4 Chapter overview 78
5 Conclusion 79
5.1 Future Works 80
References 81

Chapter 1

Introduction

High performance three-phase inverters are made nowadays with SiC transistors. These components present low losses, however, they present low thermal capacitance, and thus, high temperature variation during the fundamental frequency period of the inverter output current. This temperature variation, although having low value (some degrees Celsius or tens of degrees), happens very frequently (some tens of Hertz) and can reduce the lifetime of a power module containing these SiC transistors. As an example, Figure 1, taken from Testa et al. [2008], shows this variation for a power module using power MOSFET for automotive applications. Thus, in order to estimate lifetime of SiC power modules, fast temperature variation must be precisely estimated. This can be done by having a precise instantaneous SiC loss model, coupled with precise dynamic thermal model of the SiC dies inside the power module.

Although Wide Band Gap (WBG) components, such as silicon carbide (SiC) or gallium nitride (GaN) transistors, have higher performance than their silicon (Si) counterparts, their reliability data are either reduced or non-existent. Some works showed

Figure 1 – Number of cycles to failure versus temperature variation of a MOSFET die in a power module for automotive applications.

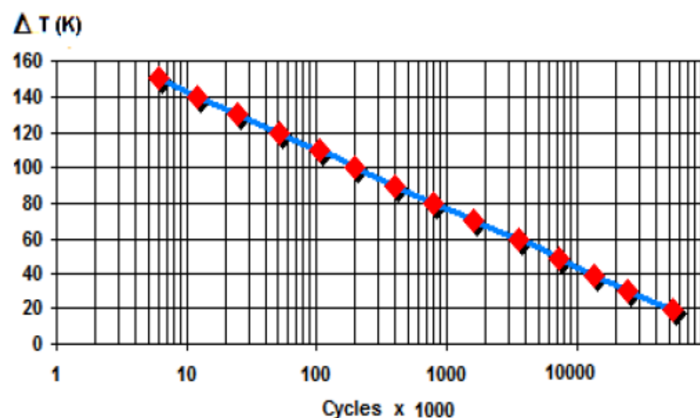

Source: Testa et al. [2008]

reduced reliability on SiC dies, when compared to Si-based switches, due to degradation of the oxide–semiconductor interface (Kaplar et al. [2012]) or the body diode characteristics (Ueda [2014]). The lack of reliability data and the general feeling in the community about the low reliability of these components are hindering their use and consequently holding back the performance of static converters.

A significant source of failure in a static converter is the power modules (Falck et al. [2018]). The reliability of a power module depends on its average temperature, which can be higher in SiC-based power modules when compared to their Si-based counterparts. High average temperature may significantly reduce the reliability of power modules (Dupont et al. [2009], Masson et al. [2011]). In addition, reliability strongly depends on thermal cycles mainly caused by the semiconductors inside (Batunlu and Albarbar [2015], Scheuermann and Junghaenel [2018]). Indeed, thermal cycles are the main source of failure in power modules, especially due to the effect of breaking the connections between the dies and bond wires, due to the mechanical fatigue caused by dilations and contractions resulting from these thermal cycles (Scheuermann and Junghaenel [2018]). This issue is even more important in SiC-based modules since the dies are smaller (for the same rated current and voltage) and, as a consequence, have lower thermal capacitance and higher amplitude of thermal cycles, which reduce reliability (Hu et al. [2017]). One of the main problems to investigate is, therefore, finding how to increase the reliability of converters based on SiC power modules, for example, by controlling thermal cycles of these components.

1.1 Objectives

1.1.1 General Objectives

The work presented here focuses on how to obtain an accurate thermal impedance model to assess the temperature variation of SiC dies in SiC power modules and in the temperature measurement of SiC dies in a real three-phase inverter during operation.

1.1.2 Specific Objectives

- Measure SiC die temperature with a infrared thermal camera for current with pulses of 1s and 1ms, in order to obtain a precise thermal impedance model and also to evaluate temperature measurement by electrical measurement (using SiC die R_{DSon});
- Create a thermal impedance model for the die for different losses and different current directions;

- Measure SiC die temperature with a infrared thermal camera in a real three-phase inverter
- Use the thermal model to calculate thermal cycles in three-phase inverter.

1.2 Published Articles

The articles below were published while working on the presented thesis:

- B. Cougo, G. Segond, A. Teixeira, L. M. F. Morais, M. Andrade, D. H. Tran,"Evaluation précise de la température de jonction des transistors SiC en dynamique pour l'estimation de la durée de vie des modules de puissance utilisés dans les onduleurs triphasé", Symposium de Génie Électrique - SGE, Lille - France July 2023.
- A. Teixeira, B. Cougo, G. Segond, L. M. F. Morais, M. Andrade, D. H. Tran, "Precise estimation of dynamic junction temperature of SiC transistors for lifetime prediction of power modules used in three-phase inverters", Microelectronics Reliability, Volume 150, 2023, 115137, ISSN 0026-2714, ⟨https://doi.org/10.1016/j.microrel.2023.115137⟩.

1.3 Thesis structure

This thesis is organized as follows:

- Chapter 2 presents the state of the art, focusing on the reliability of SiC components and temperature measurement methods of semiconductor devices;
- Chapter 3 presents a method for accurately estimating temperature variation of SiC dies used in three-phase inverters, with the aim of estimating component lifetime;
- Chapter 4 shows measured temperature variation on the metallization of "Source" terminal of SiC dies inside a power module used in a three-phase inverter for aircraft applications;
- Chapter 5 presents the conclusions of the work and proposals for continuity.

Chapter 2

State of the Art

The state of the art presented below focuses on two relevant aspects for the work. Section 2.1 discusses some elements of the current literature on the reliability of SiC semiconductors. Section 2.2 presents a study on the existing methods for measuring the temperature of semiconductors.

2.1 SiC reliability

Silicon carbide devices are relativity new if compared with silicon devices. Silicon carbide is a Wide Band Gap (WBG) semiconductor with capability to operate at higher temperature, voltage and frequency in comparison to their silicon-based counterparts and have been available to design engineers since the release of the first commercially produced SiC Schottky Barrier Diodes (SBD) in 2001 (Zverev et al. [2001]) and the first SiC MOSFET only in 2011 (First... [2011]). On the other hand, the first commercially available silicon devices (grown junction) were manufactured in 1954 (Łukasiak and Jakubowski [2010]), giving them more time to be studied and to establish themselves in the market as reliable devices. In contrast, the literature on the reliability of SiC devices is not as extensive and still requires investigation into various aspects.

2.1.1 Failure Mechanisms

A failure mechanism refers to the specific physical, chemical, electrical, or mechanical process that leads to the degradation or malfunction of a device or material over time. It is the underlying cause of a failure, detailing how and why a component fails under certain conditions. In the context of SiC MOSFETs and other electronic devices, understanding failure mechanisms is essential for improving reliability, designing robust systems, and predicting device lifetime (Valentine et al. [2015]).

2.1.1.1 Gate threshold voltage degradation

The gate threshold voltage degradation in SiC MOSFETs occurs mainly due to the smaller thickness of the gate oxide layer and the relatively higher electric field applied, compared to Si MOSFETs (Nguyen et al. [2015]). It has been shown that SiC threshold voltage increases with time when high gate voltages, +20V for the ON state and -20V for the OFF state, is applied for long periods. This can be reversed by applying an opposite gate voltage after the prolonged high voltage, for example -5V and +20V. Essentially, this implies that in switching applications where the gate voltage frequently toggles between ON and OFF states, minor variations in the threshold voltage will have minimal impact. However, for applications where the device remains in the ON or OFF state for extended durations, it is crucial to assess if changes in the threshold voltage will affect the design's performance (Nel and Perinpanayagam [2017]).

2.1.1.2 Body diode degradation

The body diode in a power MOSFET is an intrinsic parasitic element that results from its doping profile, the PN junction can be seen in the cross section of a typical SiC power MOSFET structure in Figure 2.

Figure 2 – Cross section of a typical SiC power MOSFET structure.

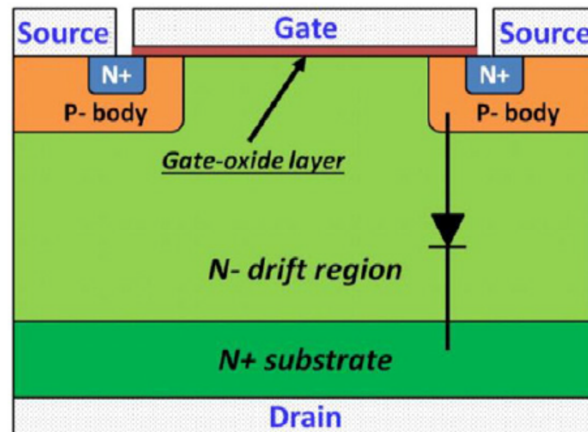

Source: Fayyaz, Romano and Castellazzi [2016].

This intrinsic anti-parallel diode is typically used as a path during dead time in a switching cell. The studies in references (Ueda [2014], DasGupta et al. [2012], Schrock et al. [2015]) have demonstrated that the body diode deteriorates under continuous forward current, leading to increased forward voltages and, consequently, higher power dissipation during conduction at a given current. Additionally, the body diode's failure during avalanche conditions has been linked to high dV/dt values during device switching, gate bias stress during the on-state, and reverse recovery processes in the body diode

(Fayyaz, Romano and Castellazzi [2016]). Two solutions to this problem can be applied, such as the addition of an external SiC Schottky Diode which has a lower forward voltage and faster recovery time to bypass the defective body diode and the addition of an n-type channel layer which provides an alternate current path for reverse currents, thus preventing degradation.

2.1.1.3 Degradation in gate leakage current

Many Switch Mode Power Supply (SMPS) designs require switching devices to handle pulse currents exceedingfour times the nominal rating, and short-circuit currents over ten times the rated current for brief periods, particularly in protection systems like DC circuit breakers (Ngwashi and Phung [2021]). SiC MOSFETs must withstand these conditions, which place significant stress on the device. During a short-circuit event, the entire DC bus voltage applies an electric field, potentially causing high leakage currents due to the gate oxide's thickness. Considering that this thickness is lower for SiC MOSFETs than for silicon MOSFETs, they are more susceptible to the reach-through effect. This degradation of the gate oxide layer worsens with repeated high current events, leading to eventual gate failure. High switching frequencies exacerbate this issue by increasing the number of pulsed current events. To mitigate this, designers must consider this failure mode in the system design or implement a gate current measurement system to monitor leakage currents and assess device health (Nel and Perinpanayagam [2017]).

2.1.1.4 Avalanche events

A significant cause of failure in systems using solid-state switches is avalanche conduction, often occurring in inductive circuit elements (Ngwashi and Phung [2021]), such as the one shown in Figure 3. This happens when energy stored in an inductive load generates a voltage spike exceeding the switching device's nominal breakdown voltage (V_{br}). To design reliable inductive switching systems, such as flyback converters, the voltage rating of the switching device must surpass the expected voltage spike. However, unexpected spikes can still occur due to stray inductances. An avalanche event causes current flow, dissipating heat and increasing the device's internal temperature. As a result of imperfections at the interface, this heat dissipation is often not distributed uniformly, which affects critical parameters like threshold voltage (V_{th}), V_{br}, and on-state resistance (R_{DSon}), impacting the module's reliability. SiC devices demonstrate superior quality compared to Si-based devices under such conditions (Ren et al. [2019]). Each avalanche event degrades the interface material layers, increasing R_{DSon} and, consequently, power dissipation during the ON state, necessitating a larger heat sink for safe operation. Therefore, avalanche mechanisms significantly influence the reliability of power electronics

systems.

Figure 3 – Example of inductive electric circuit.

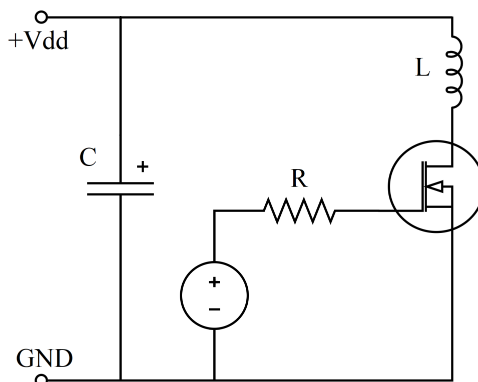

Source: Author.

2.1.1.5 Degradation under power cycling stress

During normal converter operation, the junction temperature of the device fluctuates with changes in load or environmental conditions, potentially causing reliability issues for chips or packages. SiC MOSFET package technologies follow silicon-based device designs and consist of several layers with different coefficients of thermal expansion (CTE). This mismatch and internal temperature gradients can lead to cyclic thermal stress, causing fatigue damage to the die attach-solder layer and bond wire (Wang and Jiang [2020]).

Active power cycling tests (PCT) are commonly used to assess the package reliability of Si IGBTs, and similar tests have been performed on SiC MOSFETs (Kozak et al. [2018], Ugur and Akin [2017]). Package degradations due to PCT are mainly caused by bond-wire lift-off, heel cracking (see Figure 4), delamination of solder layers (see Figure 5), and reconstruction of chip aluminum metallization. Degradation is assessed by changes in on-state voltage drop, thermal resistance, and threshold voltage. For instance, bond-wire lift-off and cracks can be detected through changes in R_{DSon}, and solder layer degradation through thermal impedance measurement.

In addition to package reliability, SiC MOSFET chip degradation under power cycling stress is a significant issue, differing from silicon IGBTs. SiC chip degradation is caused by charge trapping at the SiC/SiO_2 interface during high-temperature PCT stress (GopiReddy, Tolbert and Ozpineci [2015]). To differentiate die resistance shift from bond-wire and solder layer resistance, some studies use auxiliary Kelvin-source terminals to monitor these resistances separately. The evolution of die and bond-wire resistances shows a continuous increase in die voltage, indicating that die degradation is a major factor in SiC MOSFET degradation under PCT. Severe charge trapping effects at the

SiC/SiO_2 interface cause a large threshold voltage shift, strongly correlating with increased SiC MOSFET die resistance.

Figure 4 – Bond wire lift-off and heel cracking in a SiC chip.

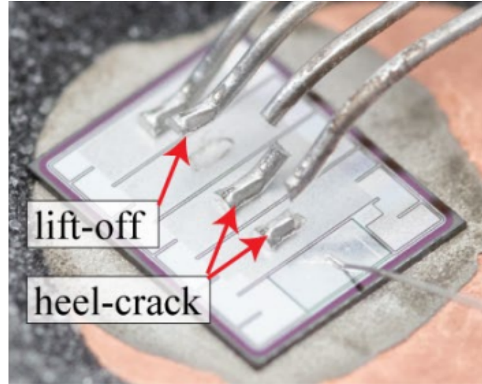

Source: Kovacevic-Badstuebner et al. [2022].

Figure 5 – X-Ray images of die attach layer: a) pre-cycling and b) post-cycling.

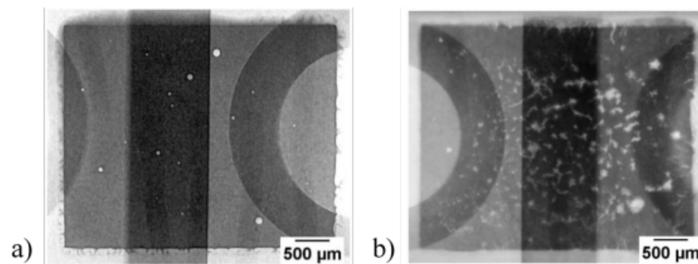

Source: Kovacevic-Badstuebner et al. [2022].

2.1.2 Lifetime models

In the field of reliability, several lifetime models exist with which the power cycling expectation can be calculated. The most common model for different packages is the CIPS 08 model (Bayerer et al. [2008]), which is based on power cycling data under various test conditions, considering factors such as temperature swing (ΔT_j), junction temperature (T_j), power-on time (t_{on}), chip thickness, bonding technology, wire bond diameter and current per bond. There is extensive research covering lifetime models for Si IGBTs, for example, power cycling tests with different load pulse durations (Scheuermann, Schmidt and Newman [2014]), lifetime estimation considering mission profiles in wind power converter (Ma et al. [2015]) and even specific to modular multilevel converters on the impact of lifetime model selection (Zhang et al. [2017]) and a mission profile-based system-Level reliability prediction (Zhang et al. [2020]).

Generally, to evaluate and quantify the thermo-mechanical reliability, power cycling tests are performed at high temperature swings (ΔT_j), such as 80K to 120K. For

much lower ΔT_j, an extrapolation is made under the respective operating conditions by means of state of the art lifetime models. The most widely used models were created for silicon IGBTs, and although it fits well for them it is not necessarily true for SiC MOSFETs. In Hoffmann, Kaminski and Schmitt [2021], it is shown that for Si IGBTs and SiC MOSFETs with the same nominal current, blocking voltage, and packaging, SiC devices have a smaller chip area, leading to significantly higher thermal resistance (R_{th}) compared to silicon IGBT modules (see Figure 6). This means that they require a lower load current I_L than silicon IGBTs to achieve the same ΔT_j. In addition, results of this work suggest that today's well-established lifetime models for power devices underestimate the lifetime of the SiC power modules for lower ΔT_j, this deviation does not lead to field relevant reliability issues.

Figure 6 – Zth characteristics of silicon IGBT and SiC MOSFET.

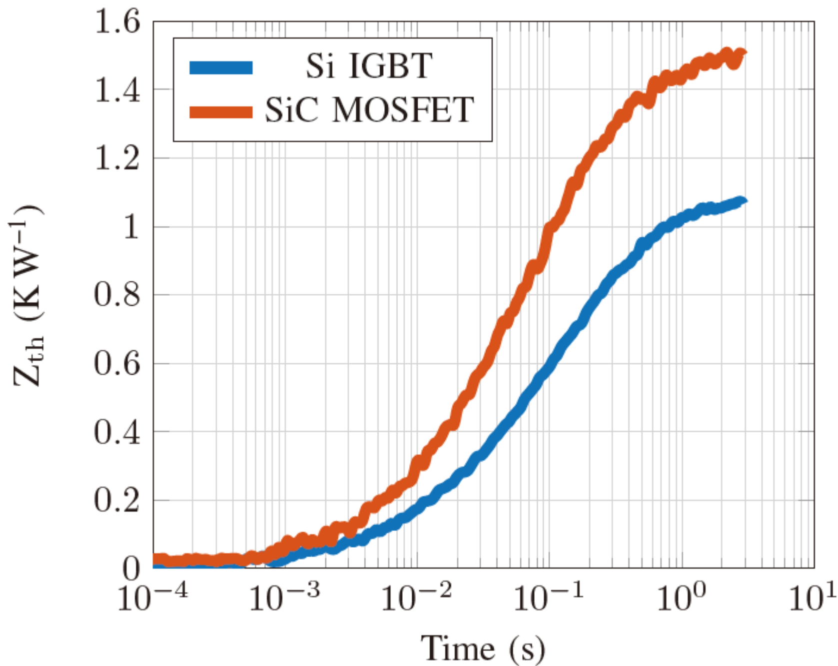

Source: Hoffmann, Kaminski and Schmitt [2021].

The study presented in Hoffmann, Schmitt and Kaminski [2023] aims to investigate the power cycling performance of SiC MOSFET power modules under low ΔT_j. Figure 7 shows the obtained results. The lifetime curve for the silicon IGBTs corresponds well with the original CIPS08 model. For the SiC MOSFETs, the lifetime curves were obtained by a parameter fit on the simplified CIPS08 model indicated by solid lines, and with a non-constant parameter to consider elastic deformation in dashed lines, obtained from Lutz et al. [2020]. The results confirm the previously mentioned discrepancy between state-of-the-art lifetime models and PCT results for power modules with SiC MOSFET chips and show that the deviation even increases towards lower ΔT_j.

Figure 7 – Power Cycling test results and lifetime models for SiC power Module.

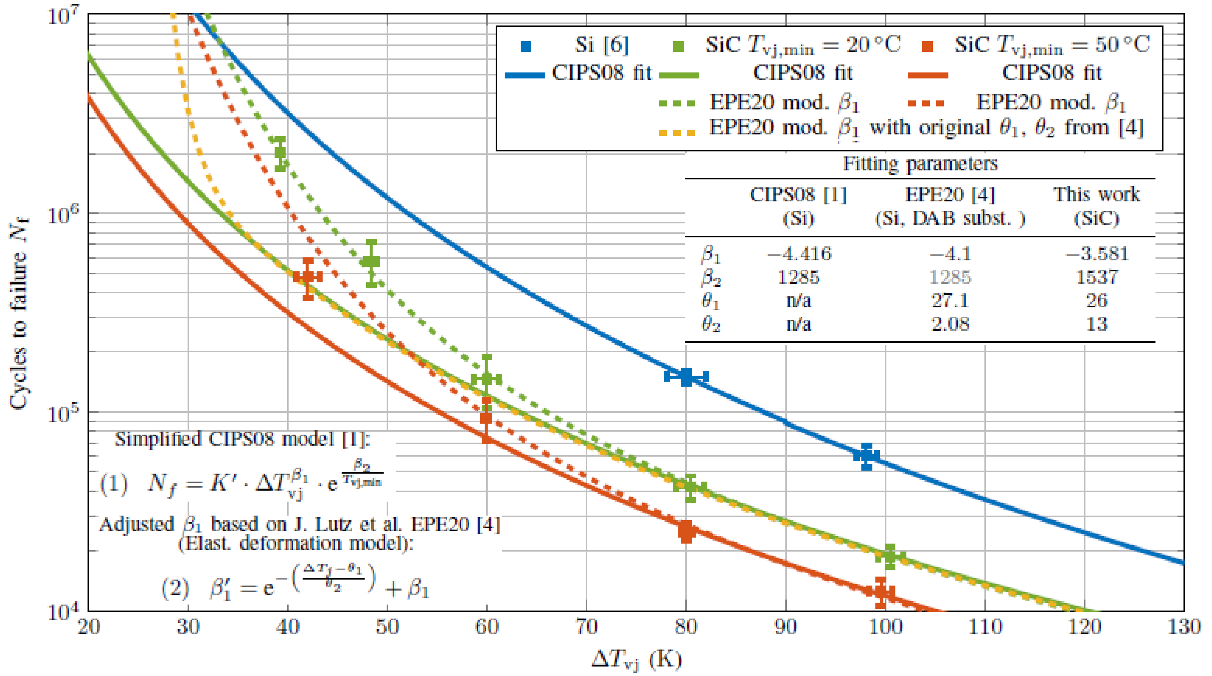

Source: Hoffmann, Schmitt and Kaminski [2023].

2.2 Temperature measurement methods

Temperature measurement of power components is important for two main reasons: for temperature management during operation and for reliability studies, as already explained in the previous section. There are three methods currently used for temperature evaluation in power semiconductor devices (Blackburn [2004]):

- Electrical methods;

- Optical methods;

- Physical contact methods.

2.2.1 Electrical methods

The electrical methods use the dependence of the selected electrical parameter on the die temperature. This parameter is called the thermo-sensitive electric parameter (TSEP). The use of the TSEP is only possible for those semiconductor dies for which the relationship between the TSEP value and the die temperature is known (Dziarski et al. [2023]). The temperature can be evaluated using only voltage and current probes on packaged devices, an advantage compared to other methods, which require either physical contact or a view of the surface. However, this method only provides a "global" temperature; it is not possible to establish a temperature map and thus know the peak

junction temperature (Avenas, Dupont and Khatir [2012]).

To date, there are several reliable temperature-sensitive parameters for Si power components, including the PN junction forward voltage (Khatir [2012]), threshold voltage (Chen et al. [2006]), bipolar transistor current gain (Yang et al. [1999]), drain–source voltage in ON-state for MOSFET (Koenig et al. [2007]), measurement of the saturation current (Nowak, Rabkowski and Barlik [2008]), monitoring of dI/dt during turn-ON (Kuhn and Mertens [2009]). For silicon carbide devices, the literature is not as extensive, and there are some particularities compared to silicon devices. Some TSEPs for SiC devices are presented.

2.2.1.1 On-State Voltage

The on-state resistance of a Si or SiC MOSFET is temperature-dependent; therefore, the on-state voltage V_{ds} is also temperature-dependent. This relationship is not linear and varies with the device. This TSEP can be used for online monitoring, however, due to its current-dependency, it requires a current measurement to decouple the load dependence from thermal effects. Many circuits have been proposed for this method of temperature measurement, in Stella et al. [2018], the circuit in Figure 8 is presented. The power module is connected in an H-bridge configuration, and supplies a purely inductive load. This simulates actual operating conditions while consuming a portion of the converted power from the input DC source. One leg of the module controls the load current and the other leg is controlled to simulate a constant voltage load.

Figure 8 – Schematic diagram of the proposed setup: Red quantities are measured online.

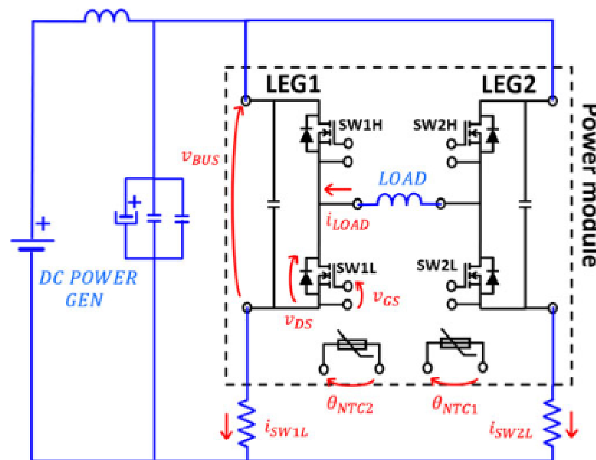

Source: Stella et al. [2018].

2.2.1.2 Threshold Voltage

The threshold voltage (V_{th}) is the minimum gate–source voltage required to switch on the device. Like the V_{th} of a silicon MOSFET, that of a SiC MOSFET decreases with temperature, typically modeled as an approximately linear dependence. There are two most commonly used methods to measure V_{th}:

1. Forcing a low current through the device with the gate and drain shorted;

2. Using a fixed low drain-source voltage and adjusting the gate voltage of the device until the required current flows through it.

One disadvantage of this method is that it can only be performed under static conditions, it cannot be used when the component is in operation due to the very fast rise times of the gate–source voltage (V_{gs}). For this reason, the quasi-threshold voltage method is often used to measure junction temperature on-line (Sharma et al. [2020]). It consists of measuring the quasi-threshold voltage (gate-source voltage at a constant current) right after the turn-on of the device by using a trigger. Figure 9 shows the schematic circuit for quasi-threshold voltage measurement.

Figure 9 – Schematic circuit for quasi-threshold voltage measurement.

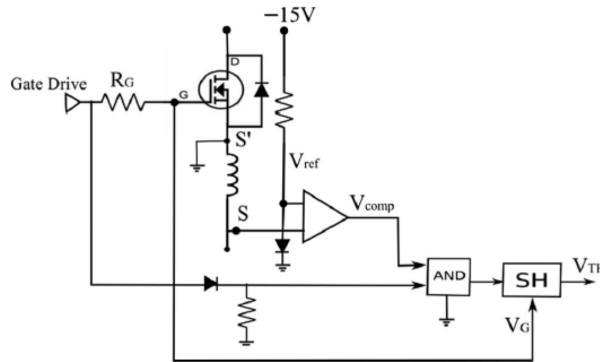

Source: Griffo et al. [2018].

2.2.1.3 Internal Gate Resistance

The internal gate resistance (R_{Gint}) of a power MOSFET is essentially the equivalent series resistance (ESR) of both the gate-to-source (C_{GS}) and gate-to-drain (C_{GD}) capacitance of the devices (Wang et al. [2018]). R_{Gint} is temperature-dependant and can exhibit a positive temperature coefficient (PTC), negative temperature coefficient (NTC) or negligible change versus temperature, depending on the device. During the gate charging process the peak of the gate current i_g can be considered proportional to R_{Gint}, so it is

possible to use a peak detector circuit for measurements. Figure 10 presents the schematic circuit for gate current peak detection.

Figure 10 – Schematic circuit for gate current peak detection.

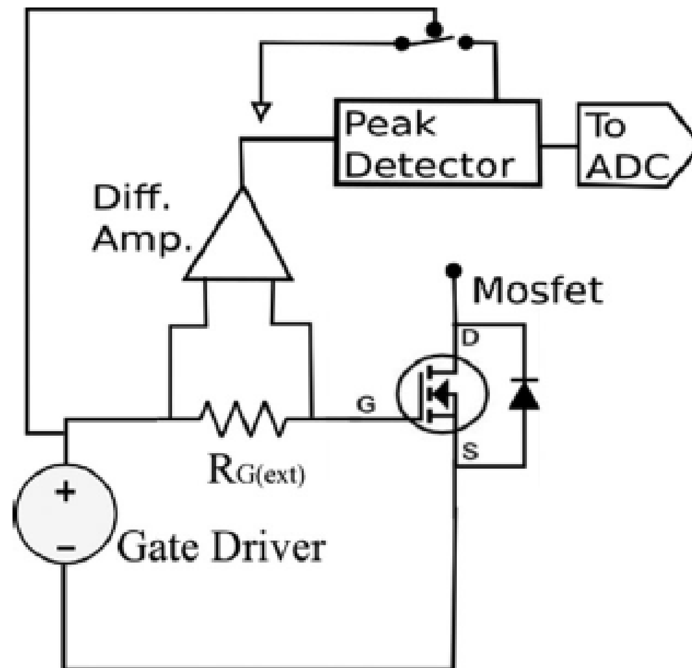

Source: Griffo et al. [2018].

2.2.1.4 Switching Rate of the Drain Current

The switching rate of the drain current (dI_{DS}/dt) is a TSEP for SiC MOSFET and can be used for junction temperature measurement. The turn-on dI_{DS}/dt linearly increases with temperature. Figure 11 shows a schematic circuit used for temperature measurement based on the switching rate of the drain current. It uses a peak detector because the voltage V'_{SS} across the source parasitic inductance L'_{SS} is proportional to the rate of change of I_{DS}. Therefore, the peak value of V'_{SS} can be used as an indirect measurement of dI_{DS}/dt. Additionally, there is an integrator to estimate the output current through the integration of V'_{SS}.

One disadvantage of this method is that high-speed switching reduces the temperature sensitivity of dI_{DS}/dt due to the presence of parasitic inductance (Gonzalez et al. [2017]). Therefore, for effective use of this method, the device should be slowed down, which increases switching losses.

Figure 11 – Schematic circuit for measurement of peak voltage and current across L'_{SS}.

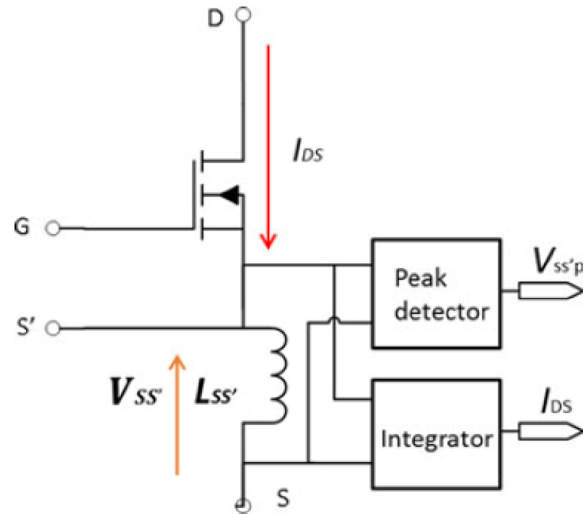

Source: Griffo et al. [2018].

2.2.2 Optical Methods

Optical methods use the impact of temperature on the optical properties of certain materials, or their response to a flow of radiation for indicating the temperature of a semiconductor device. Some of these methods are considered non-contact, which means that there is no direct contact with the tested surface and the method does not affect either the temperature distribution on the surface or the component operation. However, to analyze the temperature of the die instead of the case, it is necessary, as in contact methods, to open the case of the semiconductor element. The main advantage of optical methods is to obtain a thermal map of the component and a high spatial resolution, depending on the instrument used (Blackburn [2004]).

2.2.2.1 Luminescence

Luminescence is a phenomenon caused by external stimulation, for example, an electric field or by photo-excitation. Radiation is emitted as a result of the recombination of electrons and holes (with the peak energy occurring in direct band gap materials at the band gap energy). There are two types of luminescence: electroluminescence, through injection across a pn junction, and photoluminescence, by external optical excitation. The resolution of the photoluminescence method can be 1°C. In Blackburn [2004] it is stated that luminescence is only useful for measuring the temperature of the direct band gap semiconductors, for example, GaAs, but there is a more recent study that claims that electroluminescence contains information of the inner status of the SiC MOSFETs and can be utilized to develop junction temperature sensing methods. It is existed in all the

SiC MOSFETs and has stable characteristics (Li et al. [2019]).

2.2.2.2 Raman

Inelastic light scattering is a non-destructive optical technique which enables one to obtain information on various properties of the investigated materials (Abstreiter [1991]), the Raman method focuses on the scattering optical phonons. The local temperature of a MOSFET channel can be determined using this technique. The experimental setup is shown in Figure 12, a laser beam is focused on the gate of the MOSFET through a high-resolution microscope, and the light that passes through a specific area of the component is reflected and collected by a sensor. This light is then directed to a separator. A high-resolution Raman spectrometer is employed to determine the phonon energy of the silicon, allowing for an estimation of the temperature with an accuracy of approximately 2°C. The temperature distribution from the source to the drain is scanned to create a temperature map of the MOSFET's cross-section. The spatial resolution is around $1\mu m$, and the temperature resolution is about $1-2$°C. This method has been applied to measure the temperature of Si MOSFETs (Ostermeir et al. [1992]) and GaAs components, and also for wide band gap components like SiC (Uchida and Sugie [2018]) and AlGaN/GaN (Kuball et al. [2007]).

Figure 12 – Micro-Raman set-up (schematically).

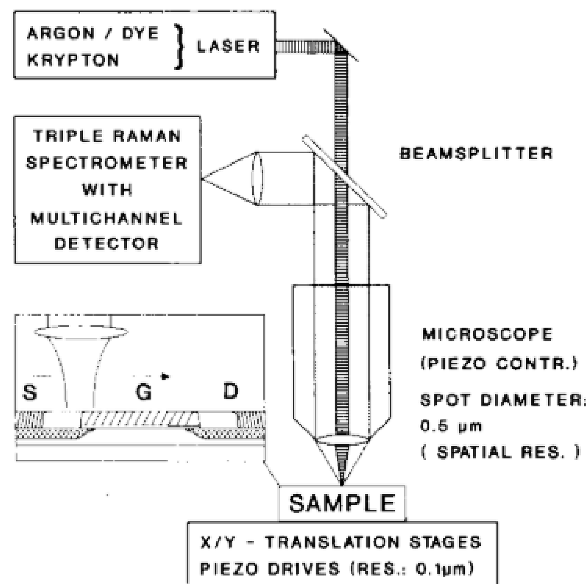

Source: Abstreiter [1991].

2.2.2.3 Thermoreflectance

Thermoreflectance is a non-contact, non-destructive method with microsecond/ nanometer resolution. It is an imaging technique that measures the fractional change in surface reflectance caused by temperature changes within the sample (Matei et al. [2020]). Figure 13 shows the measurement configuration of the thermoreflectance-based imaging technique. The light of illumination is vertically incident to the surface of the sample through optical assembly, which is vertically reflected back to the microscopic objective lens of the sample surface, and finally is received and imprinted by the CCD sensor. The device can obtain transient thermal distribution image with high spatial and temporal resolution through proper timing control of CCD exposure, illumination trigger and excitation period (Wang et al. [2021]). Thermoreflectance is a non-contact, non-destructive method with microsecond/ nanometer resolution. It is an imaging technique that measures the fractional change in surface reflectance caused by temperature changes within the sample (Matei et al. [2020]). Figure 13 shows the measurement configuration of the thermoreflectance-based imaging technique. The light of illumination is vertically incident to the surface of the sample through optical assembly, which is vertically reflected back to the microscopic objective lens of the sample surface, and finally is received and imprinted by the Charge-Coupled Device (CCD) sensor. The device can obtain transient thermal distribution image with high spatial and temporal resolution through proper timing control of CCD exposure, illumination trigger and excitation period (Wang et al. [2021]).

Figure 13 – Schematic diagram of the thermal microscopy imaging device based on thermoreflectance thermography.

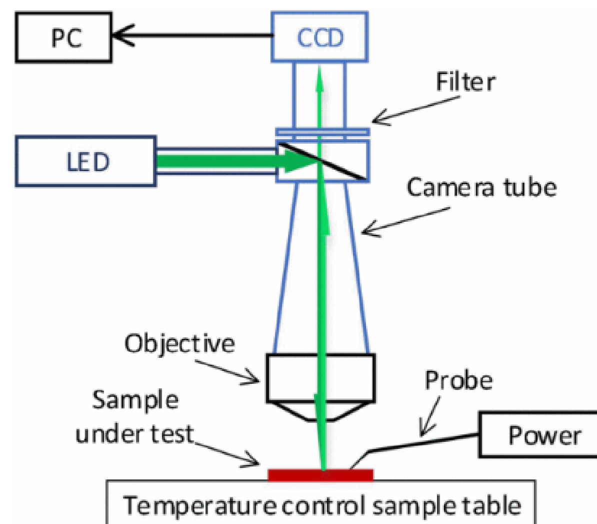

Source: Wang et al. [2021].

2.2.2.4 Infrared

Infrared imaging is a well known, well developed and most widely used optical method that is based on blackbody radiation. All physical bodies emit electromagnetic radiation which is governed by Plank's Blackbody Law, which can be simplified to the Stefan Boltzman Law when integrated for all wavelengths (Kendig et al. [2012]). The temperature of a body can be determined by measuring its total infrared radiation, which depends on the material's emissivity, ranging between 0 and 1. The emissivity for metals and other reflective objects is low, while darker objects that absorb more light are much higher. The IR method is effective when the surface being measured has an emissivity near 1. When emissivity is low, the portion of the radiated flux representing the surface temperature is diminished, and a flux reflected off the surface, influenced by the ambient temperature, is introduced. To mitigate this issue, a layer of paint with an emissivity close to 1 can be applied to the component's surface to enhance measurement accuracy.

There are different infrared techniques that can be used, such as local IR sensors, IR microscopes and the most widely used, which is the thermal camera. Two types of IR radiation detector are most commonly used in thermal cameras: microbolometer and detector based on Strained Layer Superlattice (SLS). The microbolometer is an IR detector whose resistance increases with the intensity of incident IR radiation. It is a small, uncooled sensor, usually working in the long-wave infrared (LWIR) band, and does not require cooling, broadening its application range. With a time constant of approximately 20ms, achieving high measurement frequencies (above 50 frames per second) is typically not possible. SLS detectors operate on the basis of superlattices in the LWIR and MWIR bands, with integration times ranging from 0.028ms to 0.16ms, enabling high measurement frequencies up to thousands of frames per second. These detectors provide high spatial resolution (megapixels) and show improved measurement frequency, homogeneity, and stability, especially when limited to the LWIR band. Thermograms from these detectors can be transmitted to a computer via USB or Ethernet for processing and storage. For stable measurements, thermal imaging cameras are often mounted on tripods to avoid hand vibrations and maintain a consistent distance from the observed surface.

Several studies using infrared technology for temperature measurements can be found, such as for comparison between Infrared and Thermoreflectance Imaging (Kendig et al. [2012]), closed-loop Junction Temperature Control (Ruthardt et al. [2021]), comparison beween IR camera and three TSEP (Dupont, Avenas and Jeannin [2013]), IR camera validation of IGBT junction temperature measurement via peak gate current (Baker et al. [2017]) and an ultrafast IR thermography system for transient temperature detection on electronic devices (Romano et al. [2014]).

2.2.3 Physical contact methods

Physical contact methods measure the temperature of a semiconductor die by establishing a thermal connection between the die and a temperature sensor. Some examples are thermocouples, fiber optics, scanning thermal microscopy, liquid crystals (LC), thermographic phosphor, thermistor and thermoresistor. The spatial resolution of these methods is determined by the interaction surface between the component and the probe used. Measurement response time depends on the thermal response of the probe. One of the advantages of these methods is their good spatial resolution, 30nm to 50nm has been demonstrated for scanning thermal probes (Cahill, Goodson and Majumdar [2001]). The biggest drawback of these methods is the requirement of opening the semiconductor case to place the sensor directly on the die, which is a complex process that risks damaging the component and exposes it to environmental conditions. Consequently, this method is typically performed under laboratory conditions, and the component is often unsuitable for further use afterward. In non-laboratory applications, sensors are applied to the case rather than the die, providing case temperature measurements that require additional methods to infer die temperature. Contact methods can also disturb the temperature distribution on the surface being tested and pose safety risks in high-voltage circuits.

2.2.3.1 Thermographic Phosphors

Thermographic phosphors consist of a ceramic carrier material doped with an activator, often a rare-earth metal. The method involves applying these phosphors in powder form to the tested surface, similar to the method using liquid crystals. Thermographic phosphors have luminescence properties which are very sensitive to variations in temperature and they fluoresce when illuminated with ultraviolet radiation, decreasing in intensity as the temperature increases. Several methods can be used for excitation, such as laser radiation (pulsed or continuous), particle beams, chemical reactions or thermal excitation in flames (Aldén et al. [2011]).

2.2.3.2 Thermocouple

Thermocouples are the most widely used physical contact method for measuring temperature with reasonable accuracy in both academia and industry (Jeon et al. [2022]). A thermocouple consists of two different metal or metal alloy fragments connected by a weld at one end, with the other ends free. The hot junction is the part in contact with the surface whose temperature is to be measured. The two cold junctions, which are at the same temperature, are connected to the terminals of a voltmeter and the voltage difference between them indicates the temperature of the hot junction. The advantage of using a

thermocouple is its wide temperature range (from -180°C to over 2000°C) and durability. Figure 14 shows a temperature measurement made with a thermocouple.

Figure 14 – Die temperature measurement using a thermocouple based on a representative case of TO-220.

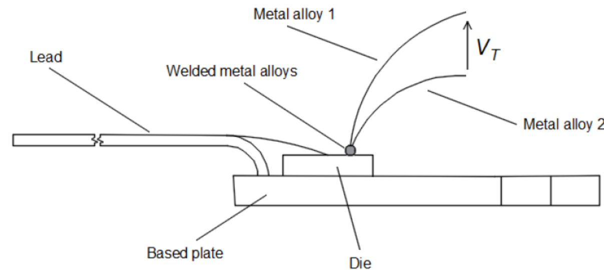

Source: Dziarski et al. [2023].

2.2.3.3 Liquid crystals

Liquid crystals (LC) change phase based on the temperature of the surface they are applied to, such as a semiconductor die. By applying LC, often in paint form, to the die, temperature changes can be visualized through different colors representing different phases. Various types of LC, including cholesteric, hysteresis cholesteric, smectic, and nematic, can be used for this purpose. The method is effective when the phase transition temperatures of the LC do not exceed the maximum allowable die temperature, allowing multiple phase transitions within the semiconductor's temperature range. Tailored LCs are available commercially in the temperature range of -30°C to 120°C with temperature bands between 0.5°C and 30°C (Azar and Farina [1997]). This technique can identify hotspots on the die, where temperatures are significantly higher than surrounding areas (Popov et al. [2007]). The nematic liquid crystal thermographic technique is nondestructive with high spatial resolution limited only by the resolution of the microscope (Park, Shin and Lee [2003]).

2.3 Chapter Overview

This chapter presented a review of SiC reliability and semiconductor temperature measurement methods. Some of the most common failure mechanisms of SiC MOSFETs were discussed, along with a brief overview of lifetime models during power cycles and the need for further studies on temperature variations smaller than 40K. Additionally, various electrical, optical, and physical contact temperature measurement methods were mentioned. Table 1 provides a summary of the characteristics of these methods. The work presented here uses the infrared method with a high-speed camera for temperature measurement in a SiC power module.

Table 1 – Advantages and disadvantages of generic methods for measuring temperature of semiconductor devices.

Method	**Examples**	**Advantages**	**Disadvantages**
Electrical	- PN Junction Foward Voltage - Threshold Voltage - Electrical Resistance - Current Gain - Infrared	- Packaged device - No contact - Potentially subsurface	- Average temperature - May require special device operation
Optical	- Luminescence - Raman - Reflectance - Thermo-optic effect - Infrared	- Temperature map - No contact - Good Spatial resolution	- Need surface view - Potentially expensive
Physical Contacts	- Thermocouple - Liquid crystals - Thermographic Phosphors - Scanning Thermal Probes - Thermistor and thermoresistor	- Temperature map - Potentially high spatial resolution	- Need surface view - Contact may disturb temperature.

Chapter 3

SiC Thermal Model

Most thermal models are represented by thermal impedance curves, which show thermal impedance of the junction to case as a function of the duty cycle of the applied losses and the pulse duration of these losses and is generally given for a single switch. However, it generally does not take into account the thermal coupling impedance between the various switches. As will be shown in Section 3.6, the model proposed does not take this coupling into account either, since thermal capacitances between different dies are sufficiently high that the variation in losses of one die in the tens of Hz range does not generate significant temperature variation in the neighbouring dies. Unlike thermal models given in the component datasheets, the thermal model presented in this chapter:

1. takes into account the variation of thermal impedance with the power dissipated by the die;
2. takes into account the variation of thermal impedance with the direction of current and the gate-source voltage of the die (MOSFET, in this case);
3. uses a fast and accurate thermal camera to determine die temperature, in place of measuring thermo-sensitive electrical values. More specifically, it measures the temperature on the source metallization of the SiC die, as this is the region having the highest reliability issue in power modules.

3.1 Thermal camera

The thermal camera used, in this work, is a X-Series Science infrared camera from Flir, model x6900sc, as it is shown in Figure 15. The camera has a thermal sensitivity of 20 mK and an operating range of -20°C to 350°C. Its maximum resolution is 640 x 512 pixels and at 320×256 pixels resolution (the one used here), it can record 2906 frames

per second. The camera connects to a computer through a Gigabit Ethernet connection, what makes it possible to use the camera along with the software.

Figure 15 – Flir thermal camera model x6900sc.

Source: Flir website.

The Flir ResearchIR is a thermal analysis software package for FLIR R&D / Science cameras. It provides camera control, high-speed data recording, image analysis, and data sharing. It has features such as thermal movie and snapshot analysis, multiple measurement analysis tools, charts and graphs, customized workspaces, image processing filters, temporal plotting, etc. Figure 16 shows the user interface of the software while being used to analyse a video, five regions are highlighted:

1. Toolboxes;
2. Main image window;
3. Temporal plot;
4. Color bar;
5. Image enhancement.

1. Camera Control Toolbox: gives the user a mini version of the camera controller where the common functions like temperature range can be selected without having to bring up the full camera controller. Object Parameters toolbox displays the current object parameters as downloaded from the camera and allows the user to edit them. Source Information Toolbox displays information about the camera or file being viewed. Source information includes data like camera type, lens used, filters, calibration ranges, GPS information, frame rate, integration time, spatial calibration data, etc. The information shown will vary depending on the data source.

2. Main Image Window: displays either live imagery from a camera or stored images and movies. By default, the image size stretched as the application window is resized. When a previously recorded movie is loaded, the movie player controls will be displayed at the bottom of the image window.

3. Temporal plots: allows the user to plot a Region of Interest (ROI) statistic versus time. The “Plot vs:” option is used to select the units for the X-axis. The width field is used to set the plot time span. This can also be done with the slider bar below the plot. If the span is less than the total data, the dark gray part of slider can be moved to display earlier data while keeping the same span.

4. Color bar: shows the relationship between the color palette and the data values in the currently selected units. The scale limits and the color distribution are controlled by the Image Enhancement Tool. The current segmentation levels are also displayed on the color bar as full width shaded regions in the currently selected segmentation colors.

5. Image enhancement tool allows the user to control the scale limits and how the color palette is mapped to the data. A real-time histogram of the data is display for each image frame so that the user can see how the data values are distributed (FLIR [2016]).

Figure 16 – Thermal camera software - Research IR.

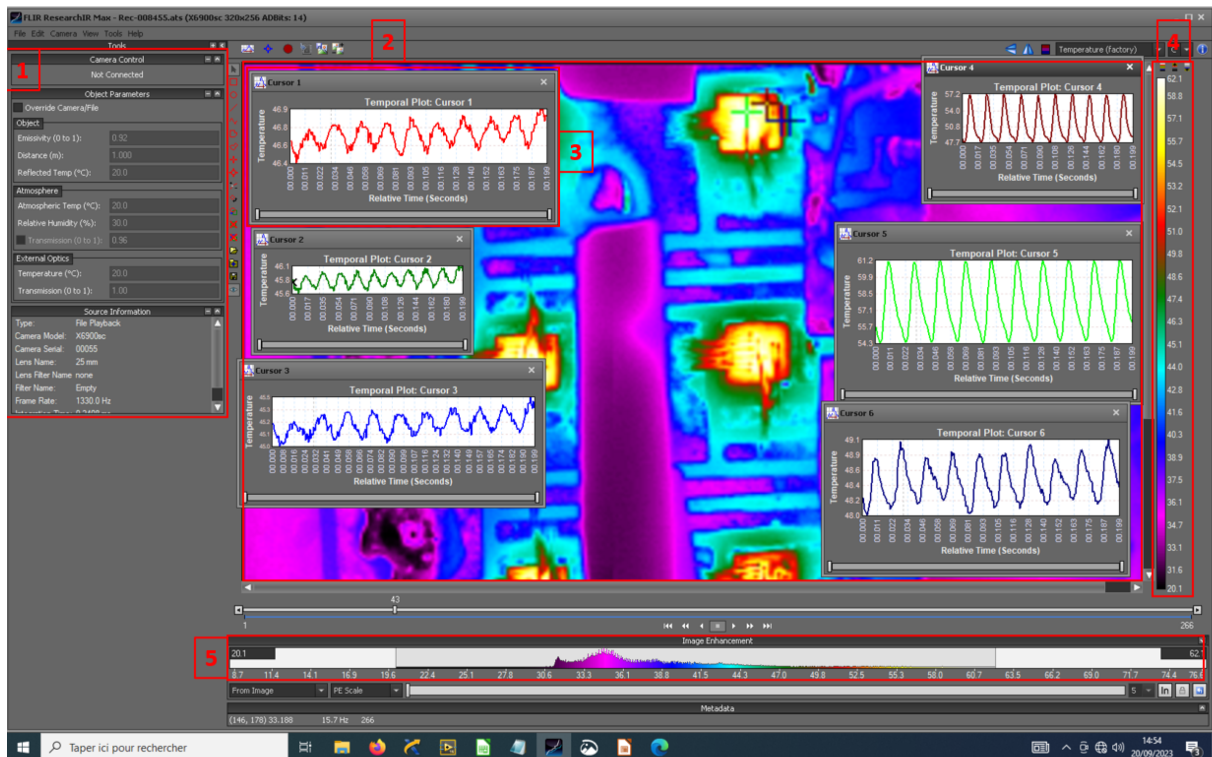

Source: Author.

3.1.1 Thermal analysis

The thermal camera provides the surface temperature of the object of interest, in this case, the SiC die. It is important to consider how the temperature will be measured since this can influence the obtained results. The SiC die is shown in Figure 17a. It can be noted that there are bonding wires covering the metallization surface, which is a factor that can influence the temperature measured by the camera, as the wire is made of aluminum and conducts current and heat differently, thus heating differently than the die's metallization.

Figure 17 – Single SiC die: (a) close-up picture, (b) thermal image showcasing different ROIs.

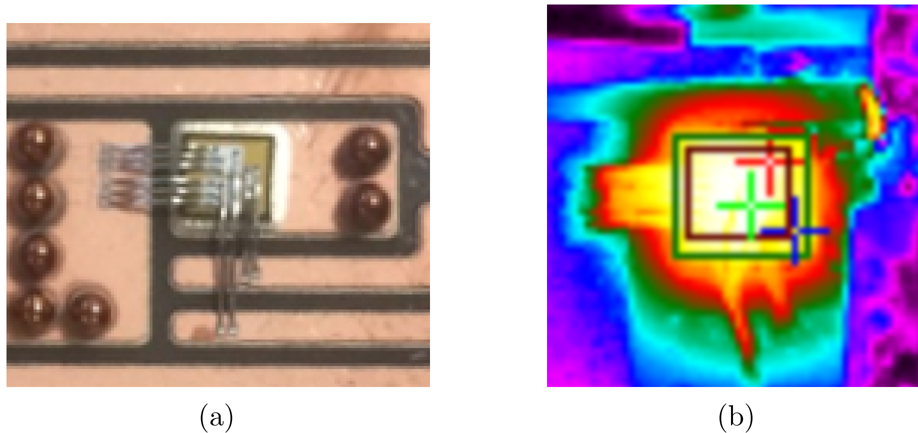

(a) (b)

Source: Author.

The camera software allows for the use of various regions of interest (ROIs) for temperature measurement. To analyze how this influences the results, a test was conducted with five different ROIs: two squares and three cursors, each 1 pixel in size, as shown in the thermal image in Figure 17b. The temperatures as a function of time in each ROI are presented in the graph in Figure 18.

It can be noted that each ROI provides a different temperature for the same current passing through the die. The temperature of the squares is given by the average temperature of each pixel within them. The larger box (green square in the image) shows a lower temperature than the smaller box. Each ROI also has different heating dynamics; some heat up faster than others and reach a different final temperature. In the following tests for calculating thermal impedance, the temperature was measured using a square the size of the die, as shown by the green box in the image. This approach is based on the assumption that the average temperature in this area better represents the temperature of the source metallization, although it also accounts for the temperature of the bond wires.

Figure 18 – Die temperatures measured by the camera for different ROIs.

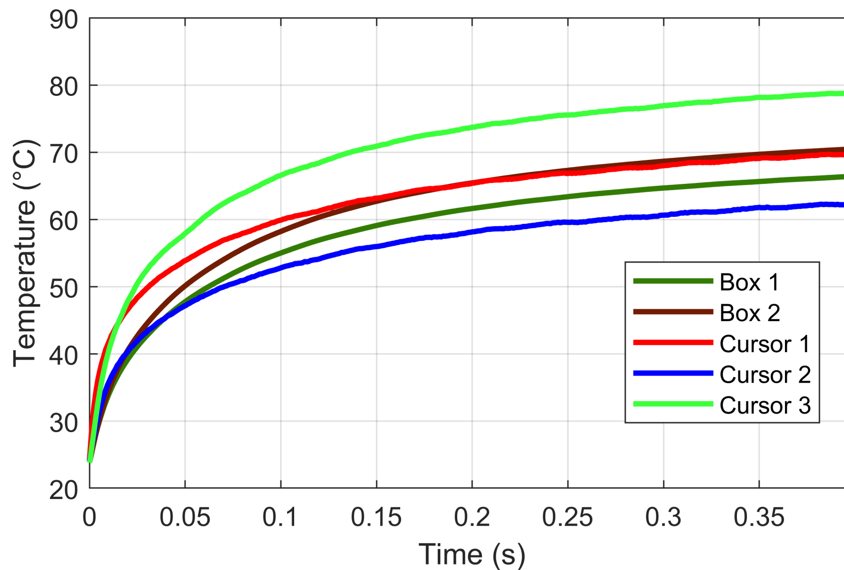

Source: Author.

3.2 Experimental setup for determining thermal impedance

The tests for determining thermal impedance were executed in half of the six-phase 540V/15kW power module presented in Cougo et al. [2020b]. As can be seen in Figure 19a, this half-circuit consists of a DBC (Direct Bonded Copper) containing six 1200 V/80 mΩ SiC MOSFETs from CREE (part number CPM2–1200-0080B) to form three switching legs. A zoom in the six SiC dies is shown in Figure 19b. The module gel filling has been removed, and all six dies were covered with a thin layer of black paint so that the die surface temperature could be seen with a fast infrared thermal camera. As in conventional thermal impedance determination, the idea is to impose constant, well-known losses on the die and measure the temperature variation in the die over time. For this purpose, the circuit shown in Figure 20 was set up in the laboratory. In this circuit, a current-limited DC supply is used to impose current in the circuit. However, given the slow current rise time in this supply (around 50ms for a current of 25A, as shown in Figure 21), the desired current must first be established in the diodes. The experimental setup for this circuit is shown in Figure 22, and the list of instruments and their features is given in Table 2.

The operating steps for characterization are given below (the waveforms are shown in Figure 23):

1. The power supply is switched on with current limiting at the desired level in order to set desired losses in the SiC die (DUT in Figure 20).

Figure 19 – SiC power module with 3 switching cells using 1200V/80mΩ SiC MOSFETs.

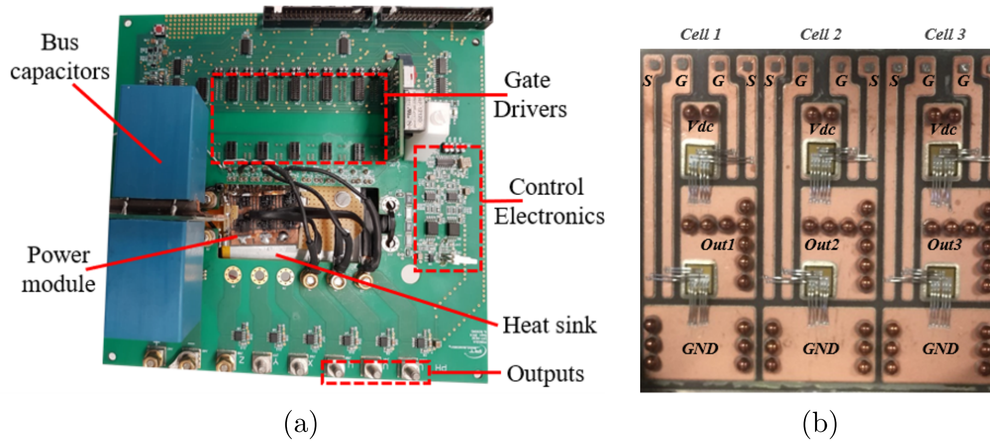

Source: Author.

Figure 20 – Electrical circuit for constant current imposition (and quasi-constant losses) on SiC dies for thermal impedance characterization.

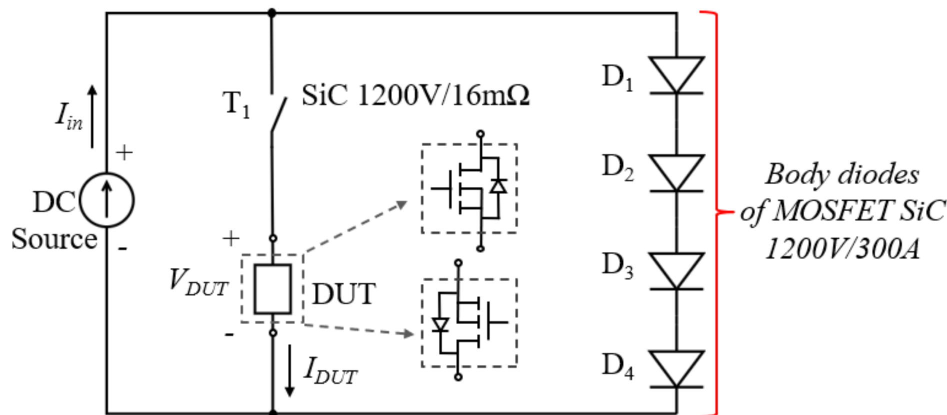

Source: Author.

2. With switch T1 (a 1200V/16mΩ SiC MOSFET in this specific case) initially turned off, the current takes hundreds of milliseconds to rise up in diodes D1, D2, D3 and D4 connected in series. These are high-current SiC diodes that practically does not heat up with currents from 0 to 30A, which must be imposed on the DUT (Device Under Test).

3. Once the supply current reaches steady state, limited to the desired current (I_{ref}), T1 is switched on. The current flowing through the diodes is transferred to the DUT. The transfer dynamics depend mainly on the resistances and inductances between the diodes, T1 and the DUT. In the case of this experimental setup, the current takes around 500μs to be stable at the DUT, as it is shown in Figure 24.

4. Current flows through the DUT for about 1s, enough time to determine the thermal impedance of the power module. The DUT current is almost equal to the current imposed by the power supply. The difference is the current in the diodes, which is very

Figure 21 – DC power suply current

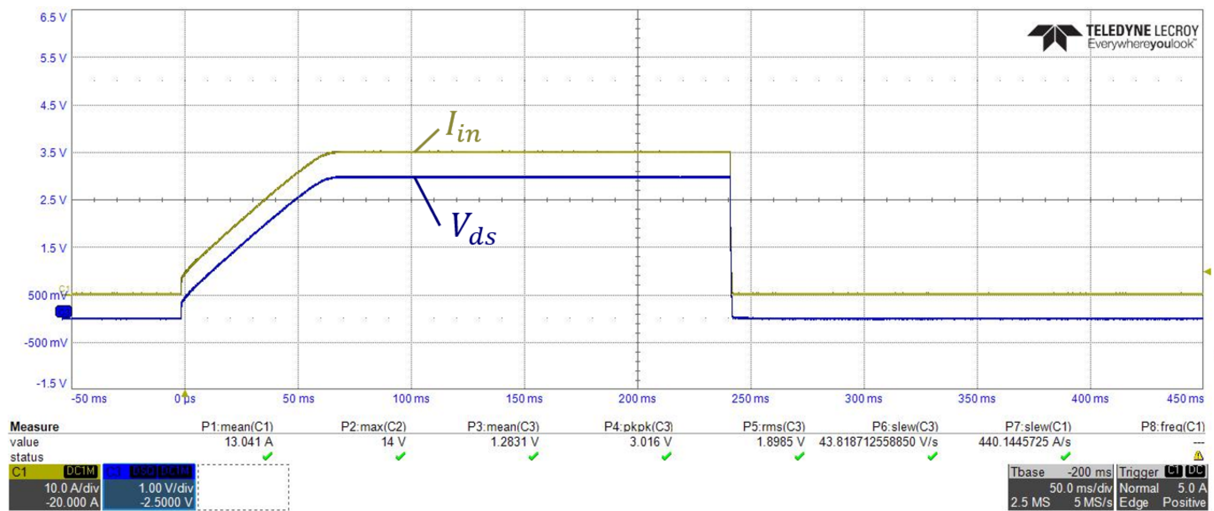

Source: Author.

Figure 22 – Experimental setup for determining the thermal impedance of SiC dies.

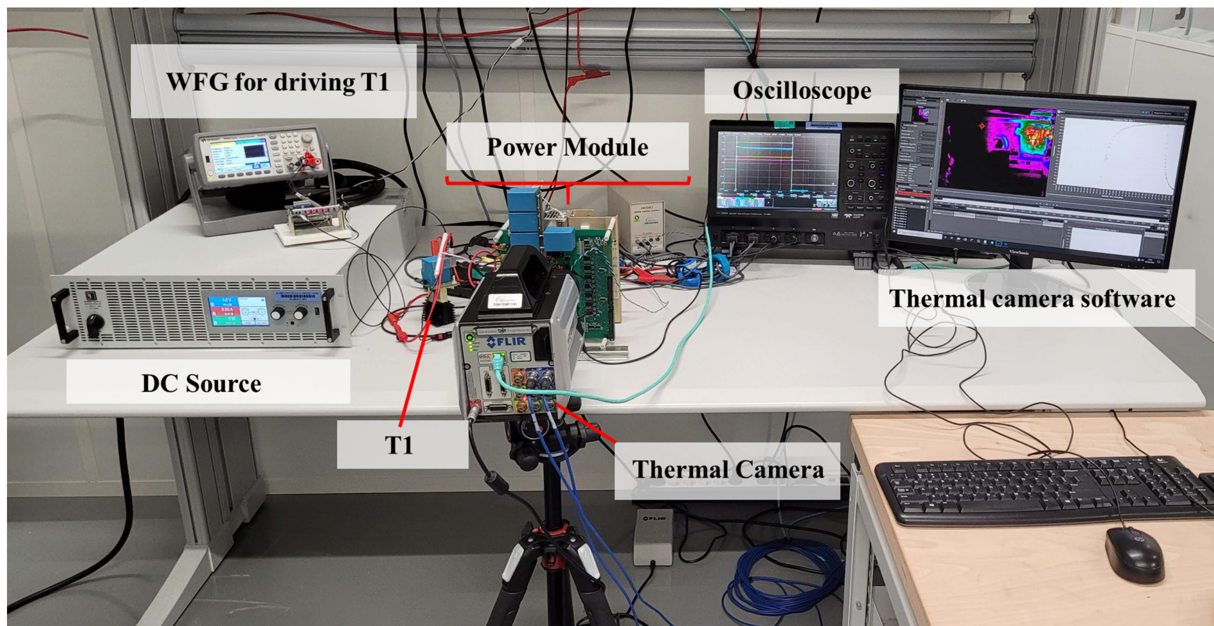

Source: Author.

small due to the voltage drop across the DUT and T1. The number (and type) of diodes to be connected in series must be adapted so that almost all the current is deviated to the DUT when T1 is switched on.

5. T1 turns off and power supply current deviated to the diodes. A few hundred milliseconds later, the power supply is switched off.

While T1 is turned on, current flows through the DUT, creating losses that heat up the DUT. These losses, for a given current level, depend on the direction of the current in the DUT and on the gate-source voltage (V_{gs}) of the DUT. In normal SiC MOSFET

Table 2 – List of instruments used in the set-up and their features.

Instrument	**Brand**	**Features**
Oscillocope	Teledyne Lecroy	HDO 6054 500MHz High Definition Oscilloscope 2.5Gb/s
DC Supply	Elektro-Automatik	EA-PSI 9750-60 0 - 750V / 0 - 60A / 0 - 15kW
Waveform Generator	Keysight	33500B Series

Figure 23 – Waveforms of currents and voltages of the components during the tests for determining thermal impedance.

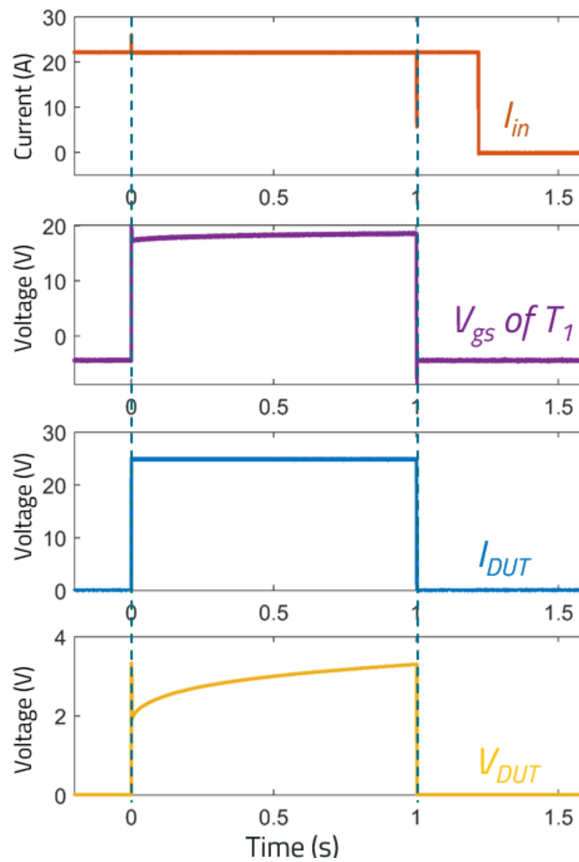

Source: Author.

operation, the following 3 cases of current conduction are possible:

- The SiC MOSFET is driven with high V_{gs} (equal to 20V for the component used in this work) and current flows from drain to source. This is referred here as "positive current" at $V_{gs} = 20$V.

- The SiC MOSFET is driven with high V_{gs} and current flows from source to

drain. This is referred as “negative current” at $V_{gs} = 20$V.

- The SiC MOSFET is turned pff with negative V_{gs} (or zero in this work), but current flows from source to drain via the body diode. This is called “negative current” at $V_{gs} = 0$ V. This mode of operation corresponds mainly to SiC MOSFETs during the dead time of a switching leg.

For each of these 3 types of operation, losses are different for a given current, and so is the associated thermal impedance, as will be seen in Section 3.5.

Figure 24 – DUT current with detail to the 500μs necessary to be stable at the DUT.

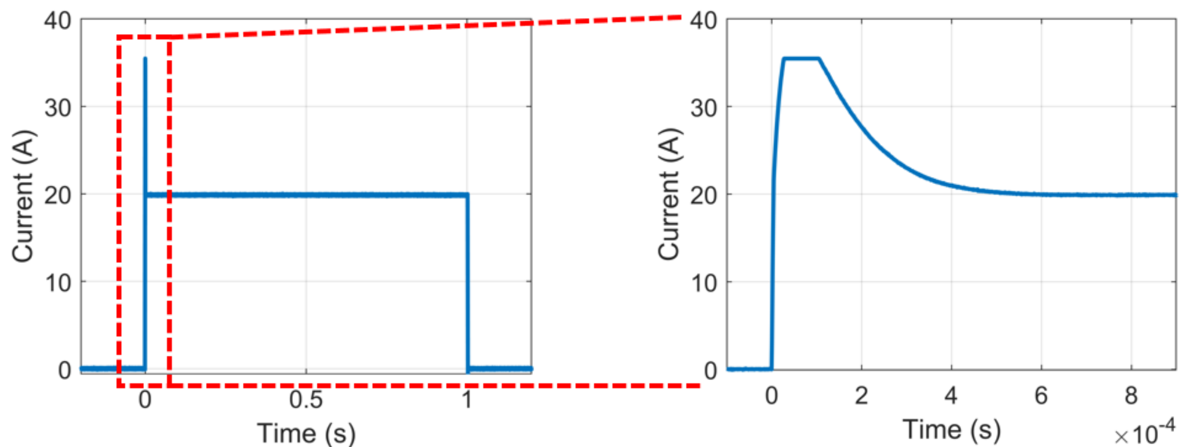

Source: Author.

3.3 Justifying the use of thermal cameras

Die temperature can be measured by three different methods, as shown in Section 2.2: optical, physical contact and electrical. Optical methods (e.g. infrared, thermo-optical effect, luminescence, reflectance, etc.) generally give a temperature map on and around the die, however the cost of the measuring equipment is high, and access to the die is required (i.e. an open power module with access to the die, without gel). Contact methods (e.g. thermocouple, thermistor, scanning thermal microscope, optical fiber, etc.) require physical contact, which can influence the measurement itself. On the other hand, these methods also provide mapping and potentially good spatial resolution. Electrical methods (e.g. direct or inverse junction voltage, threshold voltage, on-state resistance, gate current) do not require physical contact with the die (non-intrusive), but only give an average die temperature.

In the experimental setup shown in Figure 22, die temperature can be directly measured with the thermal camera, or indirectly by measuring the voltage drop across the DUT when the current flows through it. The variation of this voltage drop with temperature

can be found in the I(V) (or R_{DSon}) versus junction temperature (T_j) characteristics given in the component datasheets. Since only few curves are given in these datasheets, interpolations and extrapolations must be made to determine T_j for all voltage drops and currents measured on the component. A more accurate way of obtaining the die's I(V) versus T_j characteristic is to measure the voltage on the DUT for current pulses, with an imposed temperature measured by a thermal camera. To do this, the setup shown in Figure 22 was used. However, unlike the 5-step circuit operation shown in Section 3.2, here the current pulses on the DUT have very short durations (around 1ms) so that the DUT will not heat up while the current is flowing through it. In addition, the DUT temperature (T_j) is imposed by hot air flow applied over the DUT. Figure 25 shows the currents and voltages measured by an oscilloscope on the DUT for an applied current of 15A and temperature of 25°C. The green line represents the V_{gs}, the blue line is the V_{ds}, the yellow line is the DC Supply current and the pink line is the current on the DUT. Note that the input current takes around 500μs to stabilize at the DUT due to the transfer dynamics, which mainly depend on the resistances and inductances between the diodes, T1 and the DUT.

Figure 25 – Experimental results for current of 15A at 25°C.

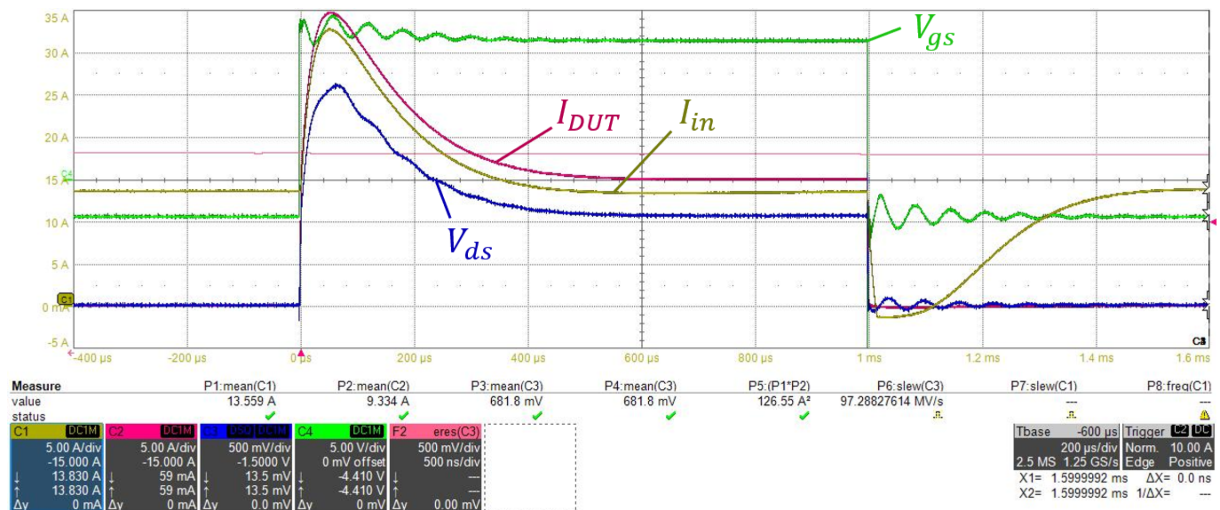

Source: Author.

To build the R_{DSon} versus T_j characteristic curves it is necessary to calculate the R_{DSon} for every desired T_j. Figure 26 shows the R_{DSon} calculated for an applied current of 15A for 25°C, 75°C and 100°C. Note that in the first 0.5ms there is an oscillation, so for the R_{DSon} versus T_j curve, a mean value of R_{DSon} between 0.52ms and 0.58ms is used. Note also, that as expected, R_{DSon} is increased with the increase of temperature.

The R_{DSon} versus T_j characteristic of the 1200V/80mΩ SiC MOSFET die in this study given in the datasheet (adapted to the die resistance measured at 25°C) and that measured by the method described above, is shown in the curves of Figure 27. Measurements were made for currents of 15A, 20A and 25A (positive and negative) on

Figure 26 – Calculated R_{DSon} for a current of 15A with a pulse duration of 1ms for 25°C, 75°C, 100°C.

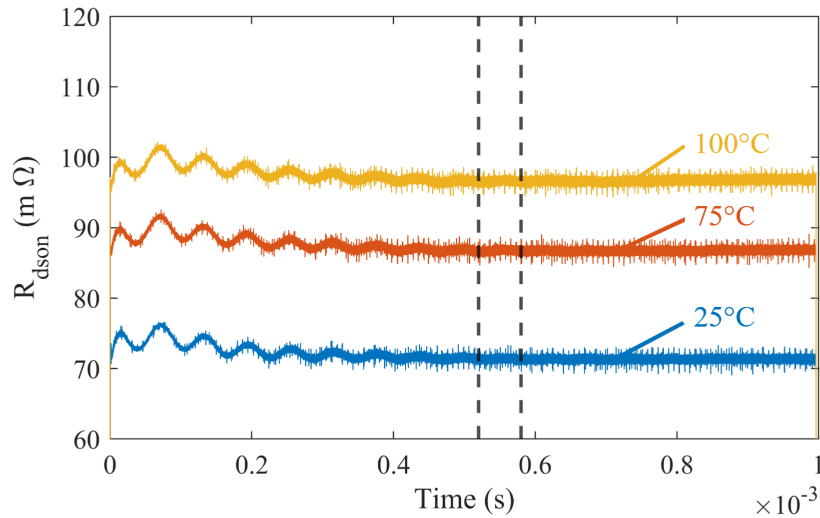

Source: Author.

the die, and for temperatures imposed between 25°C and 100°C. Note in Figure 27 that there is a relatively small difference between the R_{DSon} versus T_j characteristic given in the datasheet and measured using the thermal camera. This difference can be due to the manufacturing tolerance of the component, or by the method of measuring the component temperature: by thermal camera (in this work) or by thermocouples as is generally done by manufacturers of power components. For this reason, we will determine the thermal impedance model by direct temperature measurement using an infrared camera only.

Figure 27 – R_{DSon} versus T_j characteristic for different currents, given by the datasheet (dotted lines) and that measured with a thermal camera (solid lines), of the 1200V/80 mΩ SiC MOSFET die.

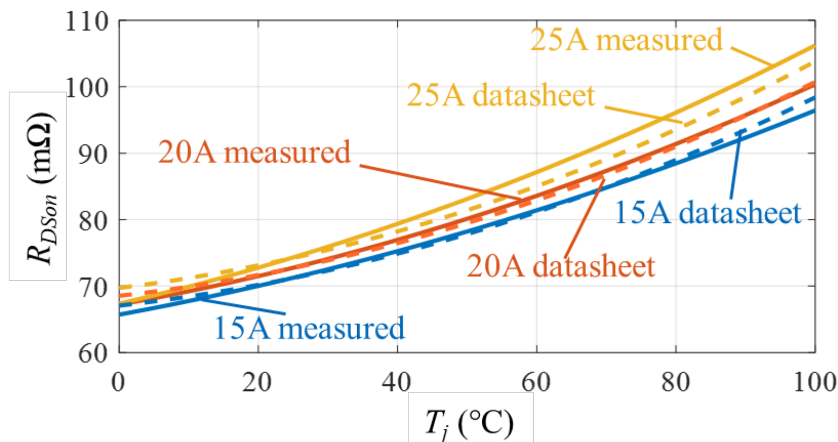

Source: Author.

3.4 Determining SiC die thermal model

The thermal model is estimated by the temperature rise curve of the die measured by the thermal camera during the 1s period that the current is imposed in the DUT, as described in Section 3.2. As an example, Figure 28 shows the applied current as well as the voltage, power and temperature measured on the die, for a current of 25A applied to the DUT. Note that, after 1s, die temperature rises from 23°C to 131°C. Its on-state resistance also rises, and consequently losses increase from 49W to 81W. To determine the thermal model, FOSTER-type model is used, which consists of a network made up of a number of parallel RC elements connected in series. The number of RC elements in series should be kept as low as possible to reduce the effort required to calculate the junction temperature, but it should accurately represents the experimental curves.

Figure 28 – Experimental results showing the time variation of the DUT temperature measured by the thermal camera, superimposed on the current, voltage and power curves measured on the same DUT, for an applied current of 25A.

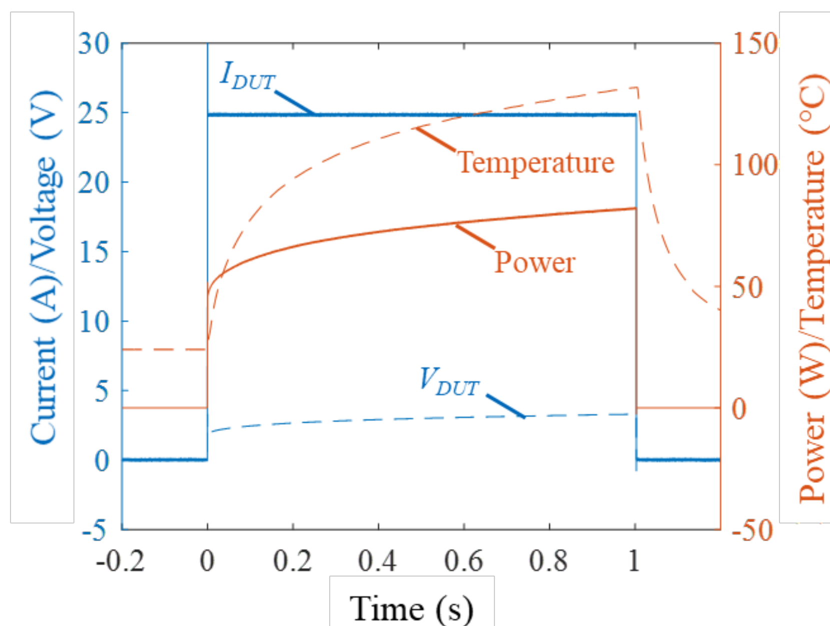

Source: Author.

Thermal resistance (R_i) and thermal capacitance (C_j) values are determined by calculating the junction temperature rise over time on this RC network, using the experimental loss curve measured on the DUT. All R_i and C_j are determined by curve fitting, in this case using the method of least squares. As an example, Figure 29 shows a thermal impedance composed of 6 parallel RC elements connected in series.

Figure 29 – Electrical circuit for constant current imposition (and quasi-constant losses) on SiC dies for thermal impedance characterization.

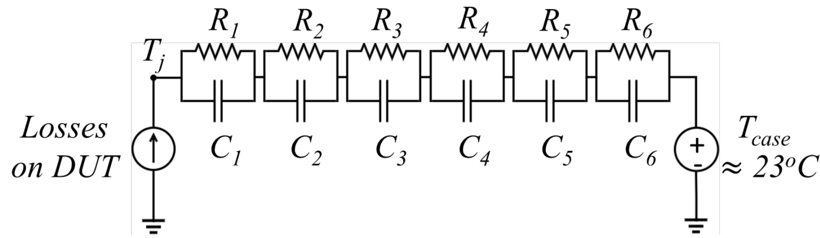

Source: Author.

3.4.1 Curve fitting

The curve fitting with the method of least squares was executed in a Excel spreadsheet. Figures 30 and 31 show a print-screen of an example of calculation for the test with current of 20A. The first thing to do is to put the time, power and temperature (measured by the camera) vectors, they are in collumns B, E and F, respectively, in Figure 30. The DeltaTemp columns calculate the temperature increase for the respective RC element at each moment in time according to the instantaneous power. In this example, there are four columns because it is a circuit with four RC elements. The temperatures for each RC element are then summed to obtain the total temperature, and the error relative to the temperature measured by the camera is calculated, represented by Tjdiff/Tj in the spreadsheet shown in Figure 31. To solve the problem, the Excel Solver tool is used, as shown in Figure 32. It employs a non-linear solution method to adjust the RC values, with a minimum constraint value, in order to minimize the percentage error, highlighted with a red rectangle. Once a satisfactory result is found, these will be the RC values for the thermal model.

Figure 30 – Excel spreadsheet to calculate the thermal model.

	B	C	E	F	H	I	J	K	L	M	N	O
9	Tempo (s)	DeltaTempo	P (W)	Tj [°C]	DeltaTemp1	Tjcalc1	DeltaTemp2	Tjcalc2	DeltaTemp3	Tjcalc3	DeltaTemp4	Tjcalc4
10	0	s	28,8944	0		0		0		0		0
11	0,00033766	0,00033766	28,8944	1,31293	0,00586593	0,00586593	0,0523371	0,0523371	0,19112236	0,19112236	1,08239345	1,08239345
12	0,00135766	0,00102	29,1264	5,27508	0,01784752	0,02371346	0,15865629	0,21099339	0,5687524	0,75987476	2,97249483	4,05488828
13	0,00237666	0,001019	29,3549	8,09094	0,01792657	0,04164002	0,15759774	0,36859113	0,53346336	1,29333813	2,10814828	6,16303656
14	0,00339666	0,00102	29,4197	10,26009	0,01794021	0,05958024	0,15596719	0,52455832	0,49839086	1,79172899	1,48766845	7,650705
15	0,00441566	0,001019	29,5972	12,01198	0,01798769	0,07756793	0,15466898	0,6792273	0,46701375	2,25874274	1,06221987	8,71292487
16	0,00543566	0,00102	29,8104	13,33673	0,01809226	0,09566019	0,1538873	0,8331146	0,4394364	2,69817914	0,77001317	9,48293804
17	0,00645466	0,001019	29,8374	14,53907	0,01804702	0,1137072	0,15179667	0,98491127	0,40918583	3,10736496	0,54246835	10,0254064
18	0,00747466	0,00102	30,008	15,48277	0,01812537	0,13183257	0,15081808	1,13572935	0,38469954	3,4920645	0,40022457	10,4256309

Source: Author.

Figure 31 – Excel spreadsheet to calculate the thermal model.

	T	U	V	W	X	AA	AB	AC	AD	AE
3										
4		1,00E-12	1,00E-12	1,00E-12	1,00E-12					0,45%
5	R	0,252	0,403	0,289	0,379				5,23205524	0,004522024
6	C	1,663	0,186	0,051	0,009					
7		0	0	0	0					
8										
9		RC 1	RC 2	RC 3	RC 4		Modelo Zth [K/W]	TjModelo	Tjdiff	Tjdiff/Tj
10		Zth [K/W]	Zth [K/W]	Zth [K/W]	Zth [K/W]			0		
11		0,000202931	0,001807259	0,006539375	0,03566731		0,044901757	1,351581	0,038651354	0,029439006
12		0,000814942	0,007217471	0,025408034	0,124273611		0,160437336	5,12937	-0,14570977	-0,027622286
13		0,001424866	0,012549526	0,042999283	0,189939336		0,251627817	8,00562	-0,085319914	-0,010545118
14		0,002033903	0,017814872	0,059431821	0,238700177		0,324645203	10,22358	-0,036514474	-0,003558884
15		0,002640863	0,023004153	0,074751874	0,274836614		0,383802864	11,98248	-0,029503448	-0,002456169
16		0,003246941	0,028128511	0,089062817	0,301670142		0,432542753	13,42015	0,083418221	0,006254773
17		0,003850951	0,033178842	0,102404908	0,321556346		0,473247749	14,59664	0,057572922	0,003959877
18		0,004454084	0,038165988	0,114868174	0,336323077		0,507852299	15,6047	0,121927412	0,007875039

Source: Author.

Figure 32 – Excel solver used for finding the best solution with minimum error.

Parâmetros do Solver

Definir Objetivo: $AE$5

Para: Máx. Mín. Valor de: 0,5

Alterando Células Variáveis:

$U$5:$Z$6

Sujeito às Restrições:

$U$5:$Z$5 >= $U$4
$U$6:$Z$6 >= $U$4

Adicionar

Alterar

Excluir

Redefinir Tudo

Carregar/Salvar

Tornar Variáveis Irrestritas Não Negativas

Selecionar um Método de Solução: GRG Não Linear

Opções

Método de Solução

Selecione o mecanismo GRG Não Linear para Problemas do Solver suaves e não lineares. Selecione o mecanismo LP Simplex para Problemas do Solver lineares. Selecione o mecanismo Evolutionary para problemas do Solver não suaves.

Ajuda

Resolver

Fechar

Source: Author.

3.5 Experimental results for determining the thermal model

This method of calculating the RC elements above will be applied to determine the global thermal impedance model of SiC dies, as shown ahead. Curves shown in Figure 28 will be obtained for a positive or negative current on the DUT equal to 15A, 20A and 25A if V_{gs} is equal to 20V (i.e. if the DUT is switched on) or equal to 5A, 10A, 15A if the current is negative and V_{gs} is equal to 0V (i.e. if the DUT is switched off but the current flows through its body diode).

3.5.1 Variation of thermal impedance with losses

Currents of different values were applied to the DUT in order to obtain the model for different power losses. Figure 33a shows these power losses for each current applied. Note that for 15A and 20A, the loss remains almost constant over the 1-second period, unlike for 25A, where the loss increases from approximately 50W to 81W in the same period. The graph in Figure 33b shows the temperature variation on the DUT for positive currents of 15A, 20A and 25A when V_{gs} is equal to 20V. The graph in Figure 34 shows curves which are a result of dividing the temperature variation by the instantaneous power, giving a sort of instantaneous thermal impedance, for the 3 imposed currents. Note that the 3 curves are close to each other, which indicates that an accurate thermal model could be used for all loss values on SiC dies. An average of these curves is used to determine the R and C parameters of the thermal model.

Figure 33 – DUT (a) losses and (b) temperature variation for positive currents of 15A, 20A and 25A.

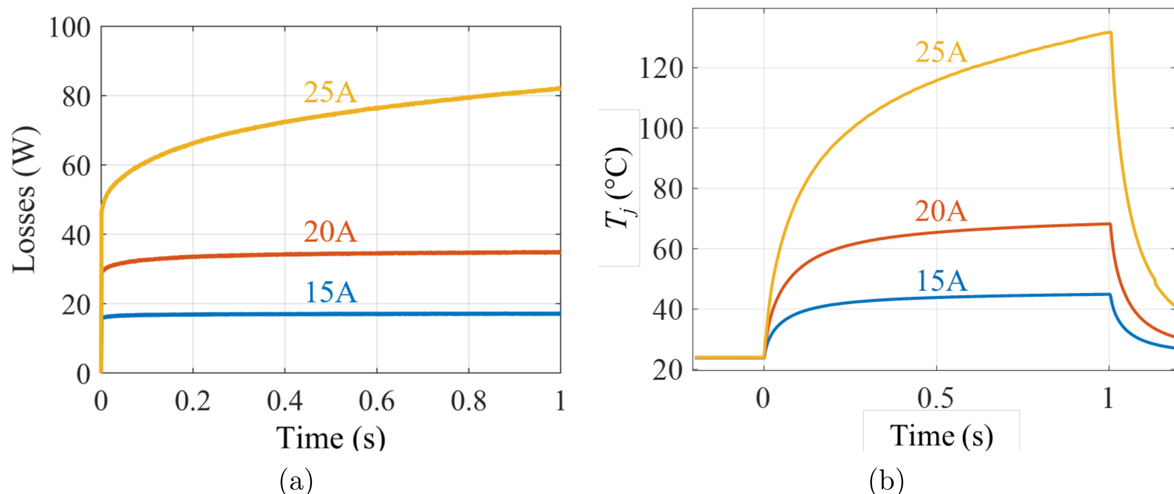

Source: Author.

Figure 34 – Instantaneous thermal impedance for 15A, 20A and 25A and applied power losses.

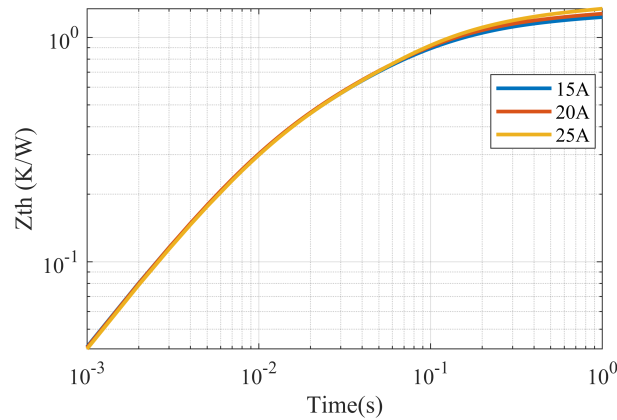

Source: Author.

3.5.2 Variation of thermal impedance with current direction

Currents of different values were applied to the DUT in the positive direction (drain to source) and in the negative direction (source to drain), when the DUT was driven with V_{gs} equal to 20V. To cover certain cases of converter operation during the dead time of a switching leg, or when the transistor is blocked but used as a diode, tests were also carried out applying a current in the negative direction (source to drain), when the DUT was blocked with V_{gs} equal to 0V. The idea was for the tests to be conducted with the same losses in each situation, however, they were not exactly the same in practice, yet close enough for the experiment to be carried out. The losses are shown in Figure 35.

Figure 35 – Instantaneous power for current applied in positive and negative directions to the DUT, and at different V_{gs}.

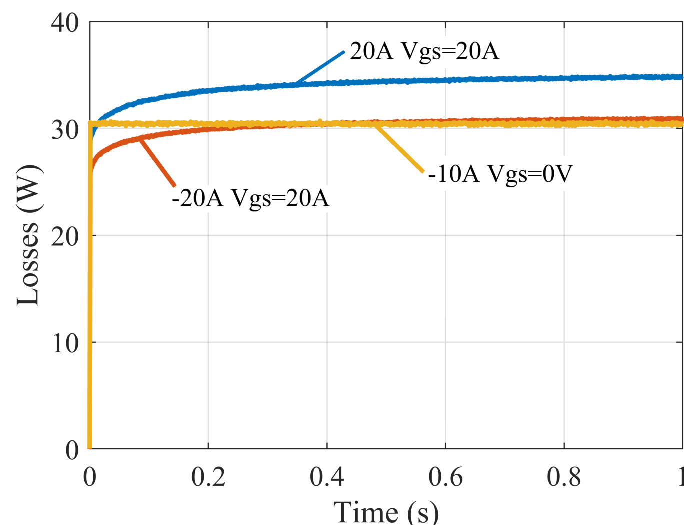

Source: Author.

Figure 36 shows 3 curves of instantaneous thermal impedance (the ratio between temperature variation and instantaneous power). Each curve is the average of curves obtained from measurements made at different values of imposed current. Each curve corresponds to a current direction and associated V_{gs}.

Figure 36 – Instantaneous thermal impedance for current applied in positive and negative directions to the DUT, and at different V_{gs}.

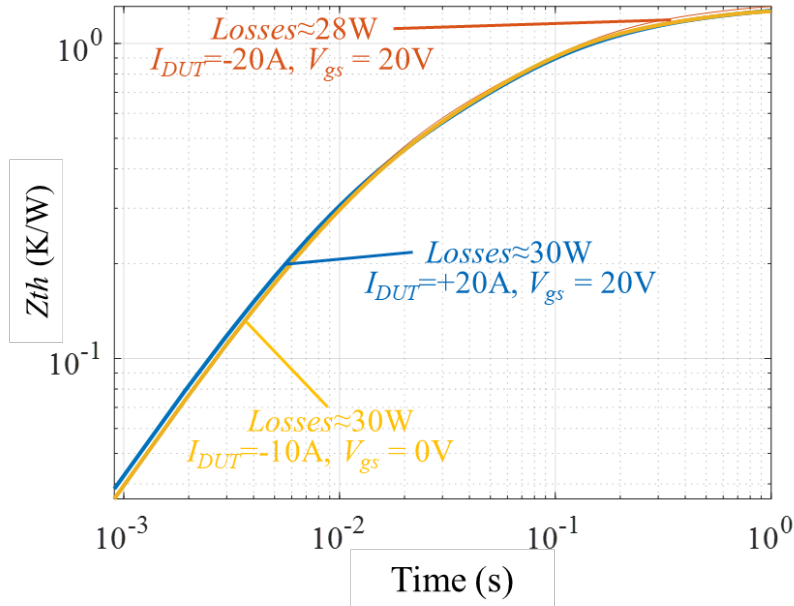

Source: Author.

Note that the 3 curves are different, indicating that the heating of the SiC die over time, for identical losses, occurs differently if the current is in different directions and for different V_{gs}. This can be explained by the region through which the current flows in these different current conduction modes, as discussed in Nguyen [2021].

- When the current is in the negative direction with high V_{gs}, the current flows through the MOSFET channel and also through the body diode, as Figure 37 shows. As a result, the current is located in a consequent volume of the die and also in a consequent volume all around the source metallization (PN junction). Not only this creates lower losses than in other current conduction modes, but since these losses are well distributed in the die volume, the equivalent thermal impedance is lower in the first few moments (up to around 25 ms), but more resistive afterwards, compared with other configurations.

- When the current is in the positive direction with high V_{gs}, the current only flows through the MOSFET channel, which is located in a substantial volume of the die (as indicated in Figure 38, but when close to the source terminals, the current concentrates in the region between source and gate. In this case, as the losses are located in a reduced volume around source terminals, it results in more equivalent thermal resistance, so the

Figure 37 – Current's path in the MOSFET when the current is negative with high V_{gs}.

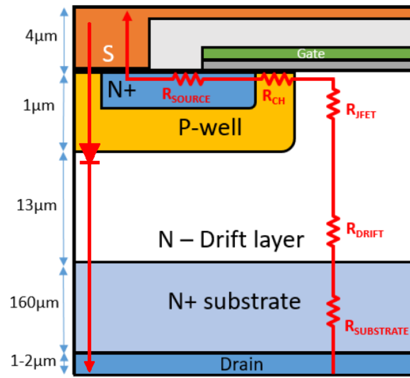

Source: Nguyen [2021].

thermal impedance is higher in the first instants, but becomes lower after 25ms than when the current is in the negative direction.

Figure 38 – Current's path in the MOSFET when the current is positive with high V_{gs}.

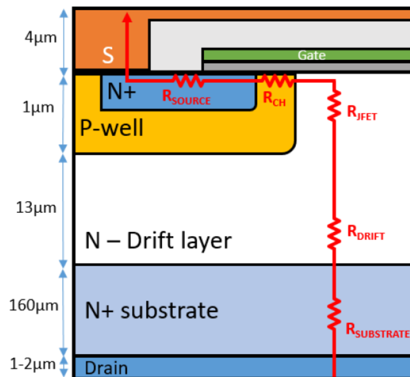

Source: Nguyen [2021].

- When the current is in the negative direction, with V_{gs} below the threshold voltage (between 5V and around 2V, in this case equal to 0V), the current only flows through the body diode, as it is shown in Figure 39. In this case, through the channel (positive current), but are concentrated in the PN junction, below the source metallization region. This region is almost as large as when V_{gs} is high. Therefore, a low impedance can be observed at both the beginning and the end of the thermal impedance curve. In summary, the current conduction mode changes the loss concentration in the regions close to the source metallization of the MOSFET, resulting in different temperature rise in the source metallization (surface visible to the thermal camera), and consequently different equivalent thermal impedances.

For this reason, the model developed in this work uses FOSTER-type thermal impedance model for each conducted current mode. The values of thermal resistances and capacitances for the 3 curves in Figure 36 are given in Table 3.

Figure 39 – Current's path in the MOSFET when the current is negative with low or zero V_{gs}.

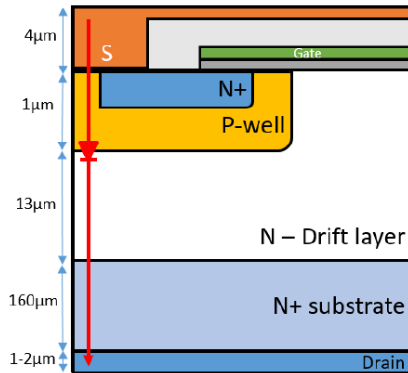

Source: Nguyen [2021].

Table 3 – Thermal resistances and capacitances values of the SiC die in a power module, for different current conduction modes.

RC elements (i)	Positive current $V_{gs} = 20$V		Negative current $V_{gs} = 20$V		Negative current $V_{gs} = 0$V	
	R_i (K/W)	C_i (J/K)	R_i (K/W)	C_i (J/K)	R_i (K/W)	C_i (J/K)
1	0.207	3.881	0.097	0.106	0.021	0.480
2	0.367	0.351	0.365	0.543	0.258	0.038
3	0.404	0.117	0.261	0.213	0.304	1.193
4	0.257	0.034	0.836	12.979	0.534	0.138
5	0.062	0.476	0.198	0.052	0.132	0.268
6	0.039	4.833	0.325	0.171	0.037	0.897

3.6 Heat-coupling effects

In a power module, proximity of dies may cause heat-coupling effects between them. In the power module of this study, a positive current of 25A was applied to the DUT (SiC die in the upper left-hand corner of Figure 19b), for 1s, as in the tests of Section 3.1. Figure 40 shows the temperature rise of the DUT measured with the thermal camera.

In this figure, the measured temperature of the 3 SiC dies surrounding the DUT is also shown. These dies around the DUT do not conduct any current and therefore have no losses. Measured temperatures are the average temperatures of all the pixels corresponding to the die surfaces. Note in Figure 40 that the dies around the DUT take $>$ 100ms to start heating up after the DUT has started heating up. The farther the die from the DUT, the longer it takes to start heating up, given the thermal impedance between the die and the DUT. Note also that, during the 1s application of a 25A current to the DUT, its temperature increased by 108°C, while that of the nearest die increased by 3.4°C. At 50 ms after the start of heating, the DUT had risen by 37°C, while the nearest die had risen by $<$ 0.1°C, a difference of over 370 times. This high difference shows that the thermal

Figure 40 – Measurement of instantaneous temperature of the SiC die (averaged over the die surface) and of the 3 neighbouring dies, for a current of 25A (positive) applied to the DUT only.

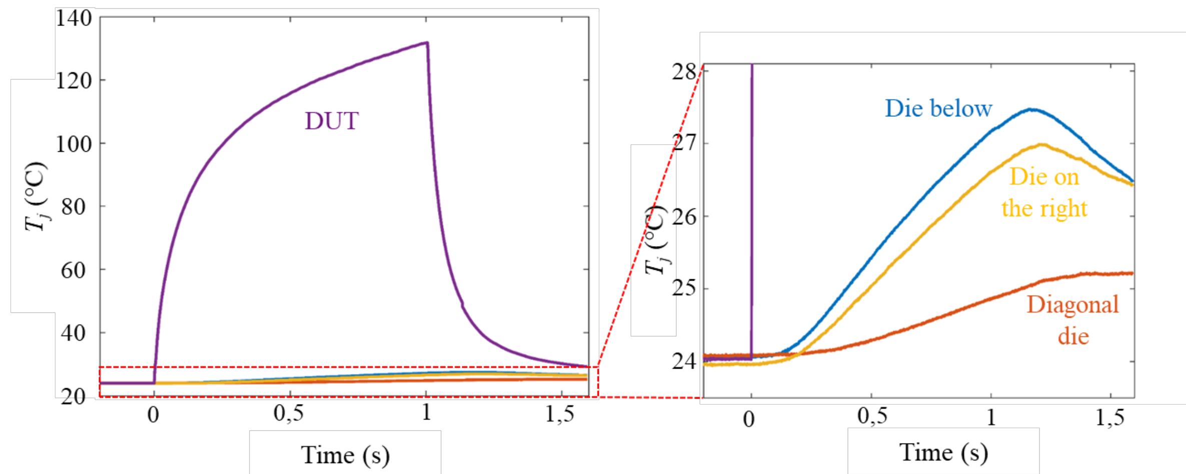

Source: Author.

impedance between the dies (due to the copper and ceramic between them) is also very high at frequencies around few tens of Hertz. However, in a power module used in an inverter application, semiconductor losses vary at a frequency equal to that of the phase current (a few tens or hundreds of Hertz). Consequently, the high thermal impedance between dies ensures that the temperature variation at the fundamental frequency of the current of a die that conducts this current does not induce temperature variation in neighbouring dies. For this reason, the thermal model developed in this study does not take into account thermal impedance between dies in a power module.

3.7 Partial validation of thermal modules

The experimental setup shown in Section 3.2 was used to validate the thermal model. For these initial tests, it was decided not to work with high-voltage switching to minimize the risk of electrical arcing inside given the lack of insulating gel around the dies. Therefore, the decision was made to impose sinusoidal currents representative of the currents that could be expected in applications such as a 540V/7.5kW three-phase inverter. A sinusoidal current from 0 to 17.6Arms is applied to a single die, which is the same one used for thermal impedance evaluation. The gate-source voltage of this die is set to 20V. Figure 41 shows the current (I_{ds}) and drain-source voltage (V_{ds}) measured on this die using an oscilloscope. It can be seen that, when the current is positive, its peak value is higher than when it is negative and that the voltage is the opposite. This is because the SiC MOSFET has lower equivalent on-state resistance for negative currents (source to drain) due to the conduction of its body diode. Consequently, losses at positive and

negative current half-cycles are slightly different.

Figure 41 – Sinusoidal current (I_{ds}, 10A/div) and voltage (I_{ds}, 10V/div) measured on the SiC die and instantaneous losses (10W/div) calculated in this die (with imposed current of 17.6Arms at 50Hz).

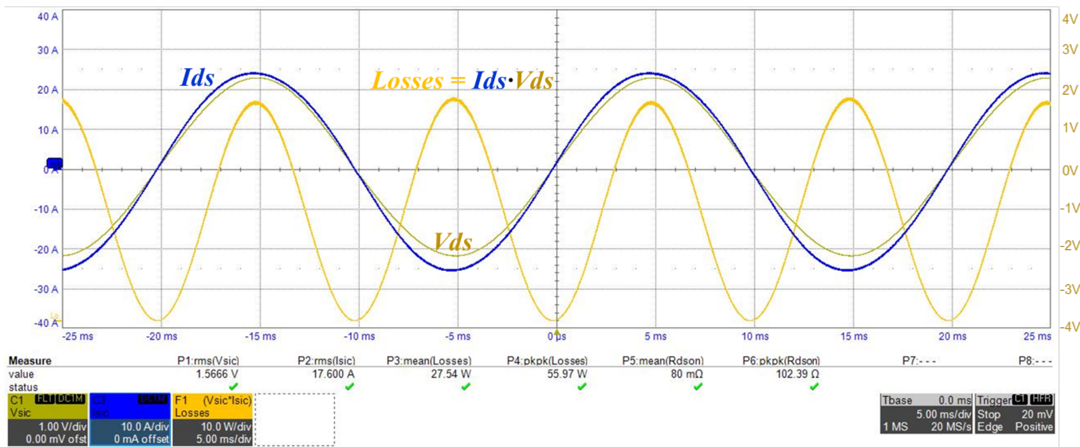

Source: Author.

Figure 42 shows measured instantaneous temperature of the die, which is calculated as the average temperature of all pixels in the square corresponding to the die, as already done for thermal impedance evaluation. In this figure, instantaneous losses in the die are also shown. It is also added to this graph the variation in die temperature calculated using measured losses and thermal impedance model for this SiC die, with parameters shown in Table 3. Note that, for the half-cycle where the current is positive, the RC network given for the current flowing in the positive direction (columns 2 and 3 of Table 3) is used. For the half-cycle where the current is negative, the RC network given for the current flowing in the negative direction with $V_{gs} = 20V$ (columns 4 and 5 of Table 3) is used.

Figure 42 shows that the measured die temperature variation is close to that calculated using the model developed in this study. Note that, although the amplitude of the losses for each half-cycle of current is practically the same, the amplitude of the temperature cycles is not. In the temperature measured by the camera, it is about 10 % higher when the current is positive, which is due to the fact that the thermal impedance of the die for a positive current is higher than for a negative current at low time (up to 25ms), as shown in Figure 36.

Temperature and loss amplitudes (ΔT and ΔP respectively) were acquired for sinusoidal currents I_{ds} from 9.6 to 17.6A (at 50Hz) and for frequencies f from 10 to 200Hz (at maximum current). The equivalent thermal impedance (Zth $= \Delta T/\Delta P$) is calculated for all points and is shown in Figure 43. In this figure, the thermal impedance is always around 10 % lower for half-cycle 2 (when current flows from source to drain).

In 43a, as expected and shown in Section 3.1, thermal impedance (Zth) does not vary significantly with current amplitude. It slightly decreases with increasing loss

Figure 42 – Temperature and instantaneous losses measured in the SiC die using, respectively, a high-speed thermal camera and an oscilloscope.

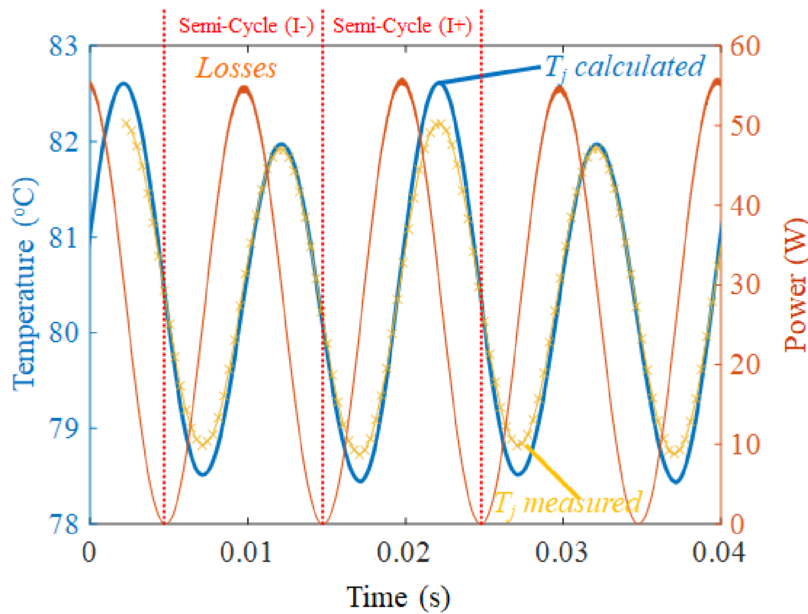

Source: Author.

Figure 43 – Calculated thermal impedance of SiC die for: (a) different current and (b) different frequencies of current applied to the die.

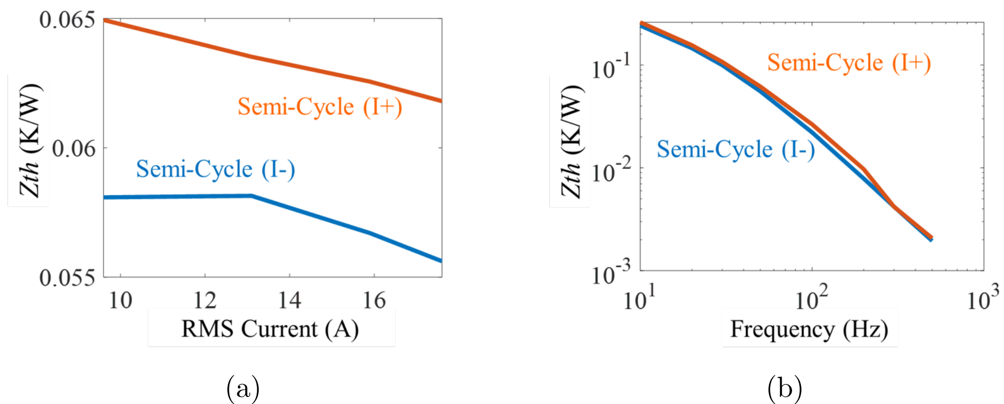

Source: Author.

amplitude. The graph at 43b shows that Zth decreases with the frequency of loss variation. This graph is given in logarithmic scale and shows that thermal impedance is relatively high for frequencies in the order of frequencies in motor currents. For example, it is around 0.2K/W for the frequency of 20Hz, which means that if there is a variation of 100W on this die at this frequency, there would be a temperature variation of 20°C, 20 times per second, which would significantly reduce the lifetime of this power module. The temperature was also measured in the dies around the die having losses. Results show that, whatever the current value (0 to 17.6A) and frequency (10 to 200 Hz), the amplitude of the thermal

cycles in the neighbouring dies is lower than the measurement noise (< 0.1°C) of the camera. This means that, as shown in Section 3.3, thermal capacity of copper and ceramic between these different dies is high enough to consider that there is no thermal coupling between the dies, concerning the temperature oscillation at the fundamental frequency of the three-phase inverter output current.

3.8 Chapter overview

This chapter presents a method for accurately estimating temperature variation of SiC dies used in three-phase inverters, with the aim of estimating component lifetime. The method is based on temperature measured with fast and accurate infrared thermal camera, for different current direction through the SiC die. It was found that the thermal impedance of the die does not significantly vary with its losses, but it does vary by 10–20% with respect to the current direction inside the die. The model developed was partially validated with sinusoidal current on the SiC die. It was observed that there is a significant temperature variation of these SiC dies having current flowing at frequencies corresponding to those in three-phase converters (some tens of Hertz). This temperature variation can significantly reduce lifetime of SiC-based modules.

Chapter 4

Temperature measurement in real three-phase inverter

Three-phase inverters are systems that include power semiconductors, capacitors, inductors, heat sinks, auxiliary supplies, small electronic components, control systems, contactors, relays, and various other parts. Some sources (Falck et al. [2018], Yang et al. [2009]) highlight that the power module is the most critical component within power electronics systems. Within the semiconductor power module, the lifetime is primarily affected by failures in die attach and bond wires (Smet et al. [2011]), resulting from the power cycling experienced by the power semiconductors.

SiC dies within power modules undergo even greater stress than traditional IGBTs. This is because SiC devices are smaller than IGBTs for the same current rating and are typically MOSFET devices, where losses are concentrated in a smaller volume. This concentration leads to higher temperature cycling amplitudes. The idea of this chapter is to show how thermal cycles in SiC dies used in three-phase inverters are significant at the frequency of the converter output current, and at the same time, validate the thermal model developed in Chapter 3. For that, tests were carried out in half of the six-phase 540V/15kW power module presented in Chapter 3 in a real three-phase inverter operation. The circuit of the three-phase inverter is shown in Figure 44.

The module is composed of three legs of identical SiC MOSFETs connected to a variable RL load emulating an electrical actuator. The switches are controlled by a Pulsed Width Modulation (PWM) through a gate driver with a resistor of 10Ω. The experimental set-up is shown in Figure 45. An oscilloscope was used to capture the 3-phase voltages and currents and the current in the DC bus. A power analyser (Zimmer LMG640) was used to measure the total losses in the inverter and also the voltage in the DC bus.

Figure 46 shows the measured current and voltage of 540V/10kW three-phase inverter in operation with switching frequency of 50kHz, fundamental frequency of 50Hz, SPWM with modulation index of 0.9 and output current of 21.11Arms and the thermal

Figure 44 – Electrical circuit of a three-phase inverter.

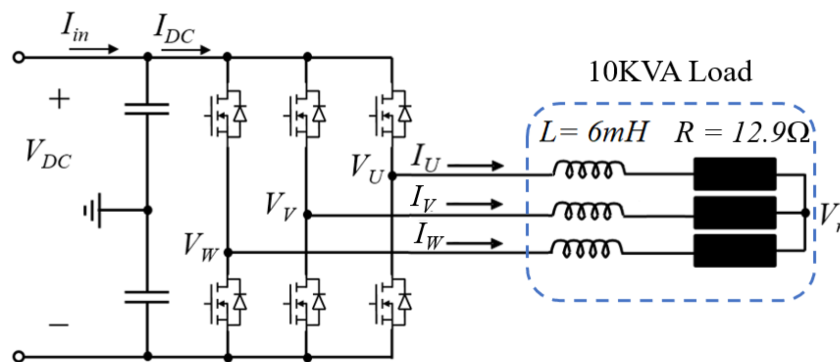

Source: Author.

Figure 45 – Set up for temperature measurement in a three-phase inverter.

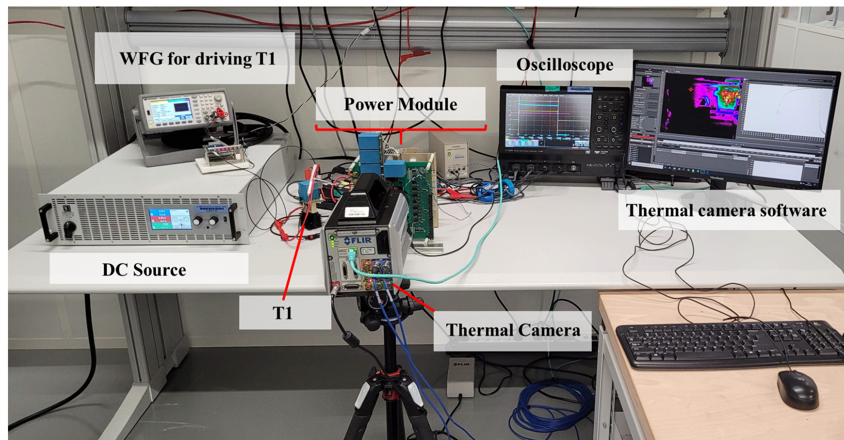

Source: Author.

image of the 6 SiC dies captured by the camera for this configuration is shown in Figure 47. It can be noted that the dies have a higher temperature than the copper. It is also observed that the bonding wires have a lower temperature than the die Source metallization, and that each die is "illuminated" differently, indicating the operation of the converter with the alternating current passing through each die at different moments. Figure 48 shows T_j in the dies of low side in each cell (leg) of the inverter, as can be noted, the temperature follows the dynamics of the current and is phase-shifted by 120 degrees between each die. Temperature analysis with the camera can be done in different ways, depending on the area being analyzed. For example, one can select which point on the surface or which area to use. As shown in Figure 49, where the black line represents a square and the rest represent different points, each has a different average temperature and ΔT_j (the waveforms were all synchronized in time for better visualization). The temperature considered was the average of the temperatures of each pixel within the square placed around the perimeter of the die.

Figure 46 – Measured current and voltage of 540V/10kW three-phase inverter, having total losses of only 212W.

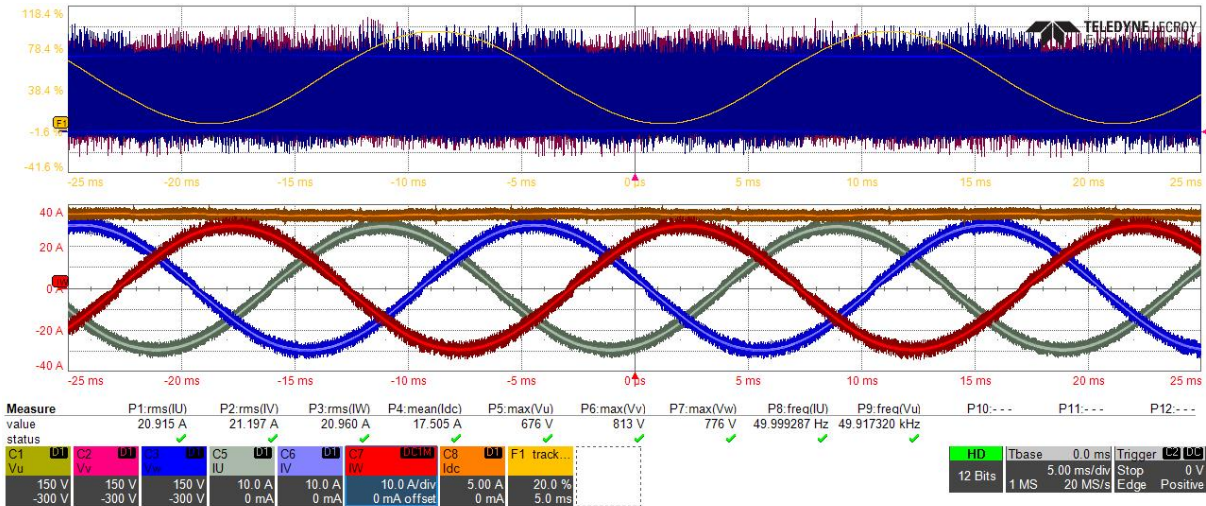

Source: Author.

Figure 47 – Thermal image of SiC power module at $V_{DC} = 540\text{V}$, $f_{fund} = 50\text{Hz}$, $f_{sw} = 50\text{kHz}$, $M_i = 0.9$ and $I_{out} = 21.11\text{Arms}$.

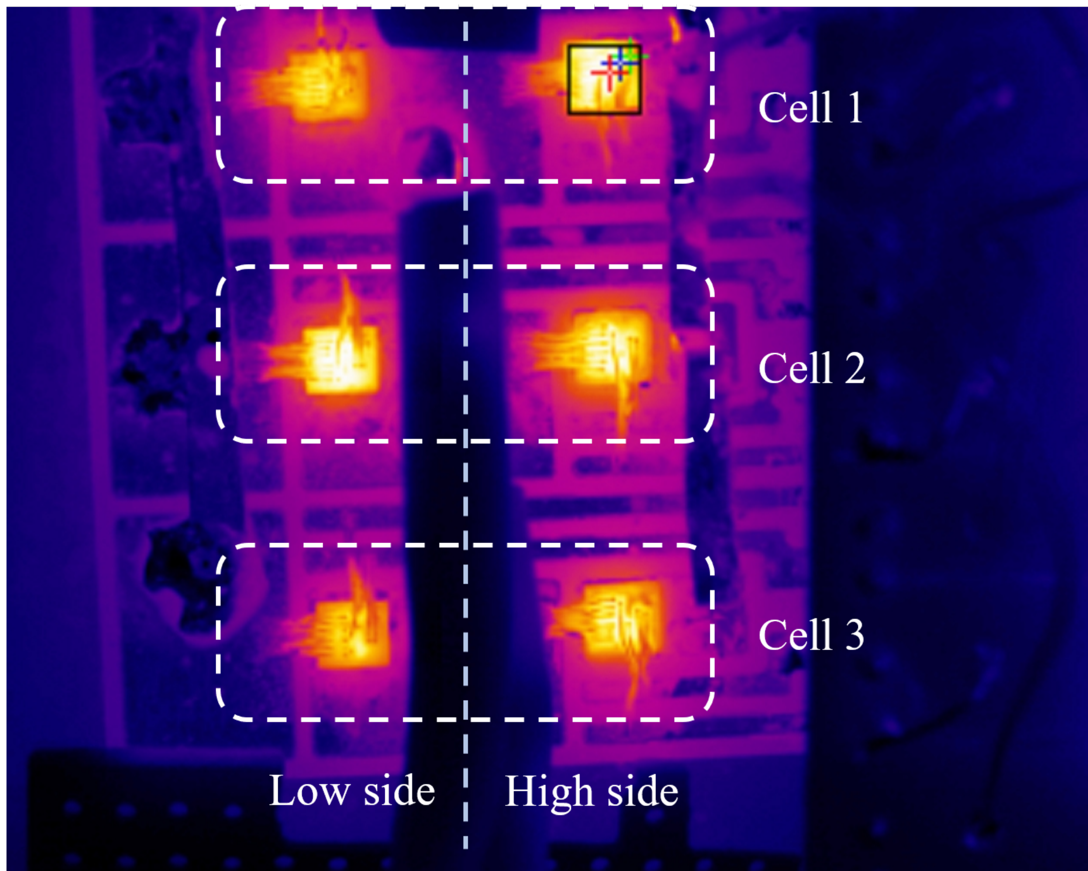

Source: Author.

Figure 48 – Temperature measurement of SiC dies of the low side in three different legs of the inverter with f_{fund} = 50Hz, f_{sw} = 50kHz, M_i = 0.85, I_{rms} = 14.73A and SPWM method.

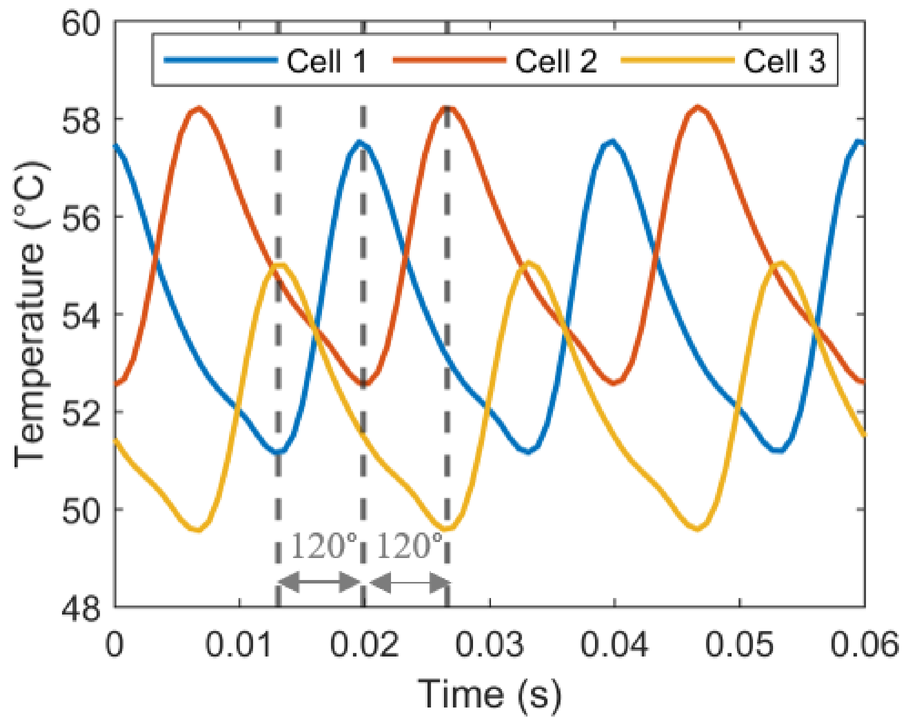

Source: Author.

Figure 49 – Temperature measurement of different points in the same SiC die with f_{fund} = 50Hz, f_{sw} = 50kHz, M_i = 0.9, I_{rms} = 21.11A and SPWM method.

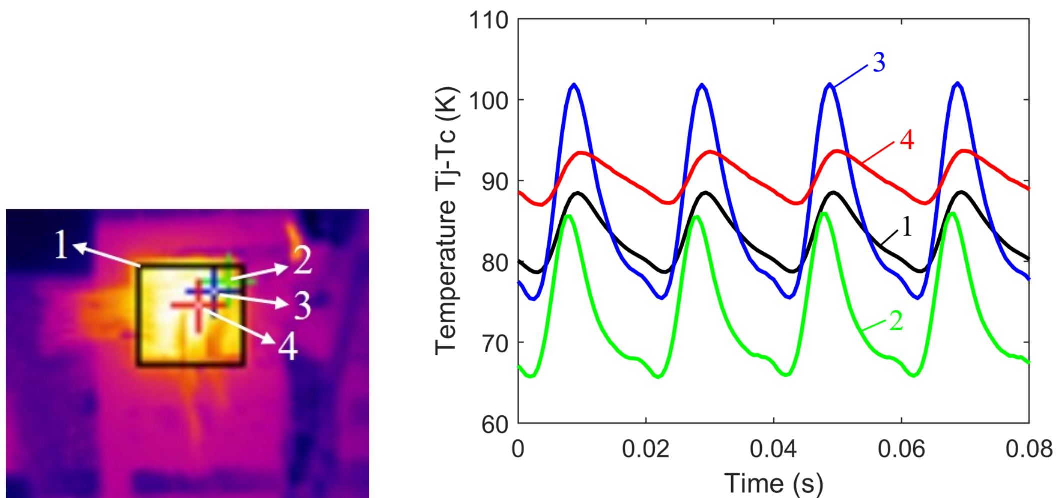

(a) Points of measurements.

(b) SiC die temperature.

Source: Author.

4.1 Parameters Variation

The nominal operating parameters were chosen to meet the requirements of aircraft applications, as presented in Table 4. The goal is to measure the die's temperature under different loads, modulation indexes, PWM methods, fundamental frequencies, and switching frequencies, and to compare these with the temperatures calculated using the proposed thermal impedance model. Since the power module does not have isolation gel, tests with the inverter began at a low DC bus voltage and was gradually increased to the nominal voltage of 540V without any insulation issues.

Table 4 – Parameters for inverter nominal operation.

Parameter	**Value**
f_{sw}	50kHz
f_{fund}	50Hz
R_g	10Ω
Modulation Index	0.9
V_{DC}	540V
$I_{out,rms}$	14.64A

4.1.1 Load Variation

The first test was conducted to assess the impact on temperature variation in response to load variation. The fundamental and switching frequencies, modulation index, and DC voltage were kept constant, and the temperature was measured for ten different load values. Table 5 shows the values of the output current, input power, output power, and total losses.

Table 5 – Values of current, input power, output power and total losses for load variation (* Decrease in losses probably caused by a measurement error).

Load (kVA)	$I_{out,rms}$ **(A)**	P_{in} **(W)**	P_{out} **(W)**	**Losses (W)**
0.0	0.47	63	23	40.36
2.8	2.63	1533	1413	120.24
5.6	5.09	2782	2650	131.60
8.4	7.64	4047	3906	141.70
11.2	9.99	5175	5030	144.80*
14.0	12.40	6295	6154	141.30*
16.8	14.64	7307	7164	143.06
19.6	16.88	8315	8158	157.67
22.4	18.98	9243	9065	178.40
25.2	21.11	10168	9956	212.40

Source: Author.

As expected, losses increase with load because more current passes through the MOSFETs. Despite the observed decrease in losses between the 11.2kVA and 14kVA loads, likely caused by an error in the measurement device. Figure 50 shows the temperature measured on the SiC MOSFET die. The temperatures were synchronized and adjusted from their average values for comparison. It is noted that temperature variation amplitude also increase with load, going from $\Delta T_j = 0.86$°C at 2.63Arms to $\Delta T_j = 14.58$°C at 21.11Arms.

Figure 50 – Junction temperature variation for load variation.

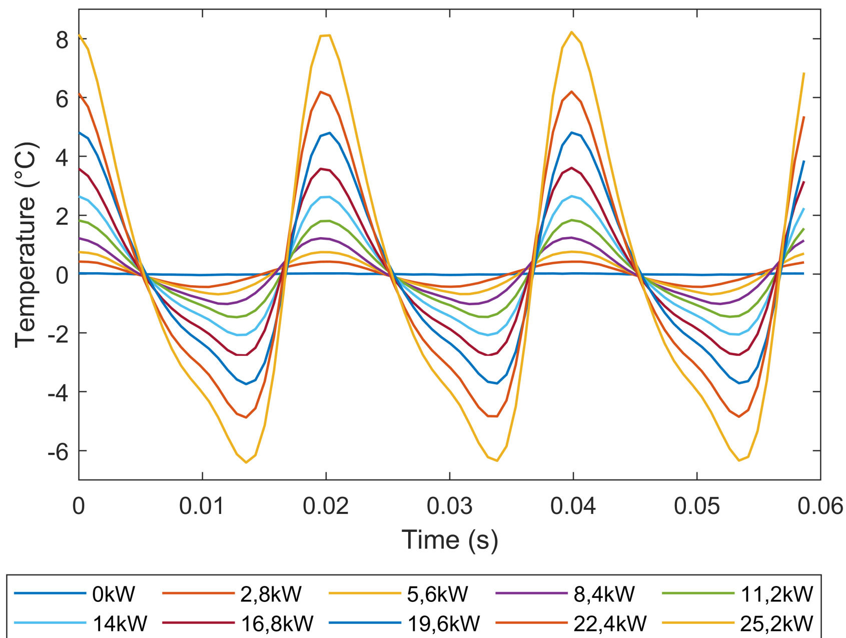

Source: Author.

4.1.2 Modulation Index Variation

For the tests with modulation index variation, the load had to be adjusted in each test to maintain the nominal current values, approximately 14.75Arms. The fundamental and switching frequencies and DC voltage were kept constant, and the temperature was measured for nine different modulation indexes. Table 6 shows the values of the input power, output power, and total losses. It is believed that a measurement error occurred regarding the losses, as they were expected to remain nearly constant irrespective of the modulation index, as shown in Cougo et al. [2020a]. Figure 51 shows the expected behavior of losses concerning the modulation index. The temperature variation is shown in Figure 52. The amplitude increases as the modulation index rises because conduction losses become more uneven between the positive and negative half-cycle currents.

Table 6 – Values of input power, output power and total losses for modulation index variation (* A measurement error likely occurred, as the losses were expected to remain nearly constant).

Modulation Index	P_{in} (W)	P_{out} (W)	Losses (W)*
0.900	7354	7207	146.71
0.790	6477	6309	167.29
0.703	5743	5554	189.13
0.635	5182	4977	205.59
0.582	4733	4513	219.60
0.540	4380	4148	232.00
0.506	4095	3852	242.25
0.450	3608	3352	255.86
0.357	2758	2482	275.93

Figure 51 – Semiconductor losses versus modulation index.

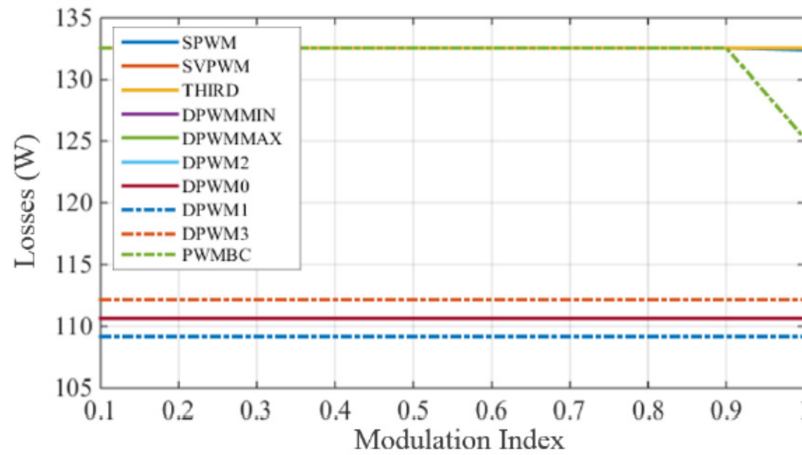

Source: Cougo et al. [2020a].

Figure 52 – Junction temperature variation for M_i variation.

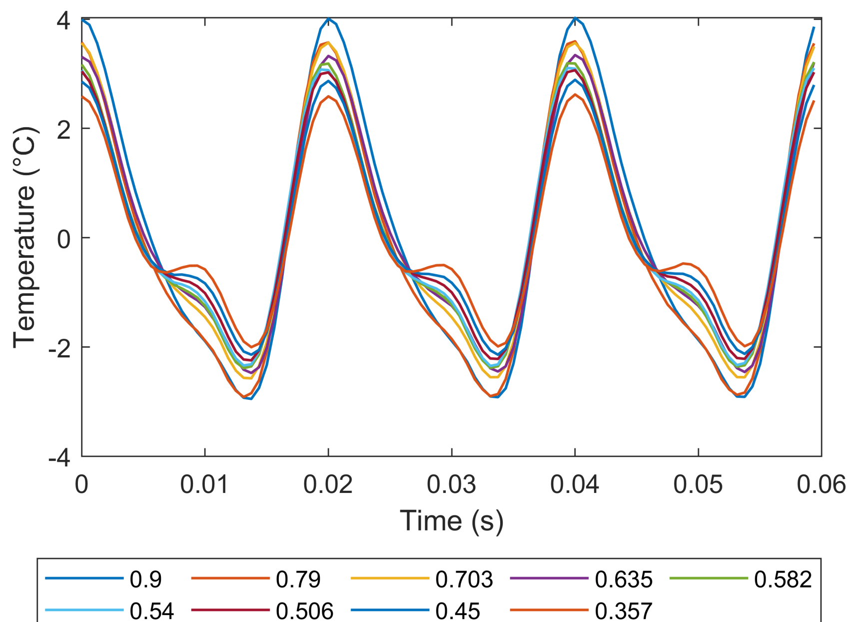

Source: Author.

4.1.3 PWM Method Variation

There are different PWM methods, many can be found in Hava, Kerkman and Lipo [1999]. They are commonly divided into two categories, as continuous PWM (CPWM) and discontinuous PWM (DPWM) methods. In continuous methods, the modulation waves remain within the triangle carrier peak boundaries, and during each cycle, the triangle and modulation waves intersect, resulting in on and off switchings. In discontinuous methods, the modulation wave of a phase includes at least one segment that is clamped to the positive or negative DC rail for a total of up to 120°, meaning that during these intervals, the corresponding inverter leg ceases modulation. Since no modulation leads to no switching losses, the switching loss characteristics of CPWM and DPWM methods differ.

Tests were conducted for six PWM modulation methods: Space Vector PWM (SVPWM), Sinusoidal PWM (PWM) and Discontinuous PWM methods (DPMIN, DP-MAX, D0 and D1). The modulation waveforms of these six methods can be found in Figure 53.

Figure 53 – Modulation waveforms of the modern PWM methods (M_i = 0,7).

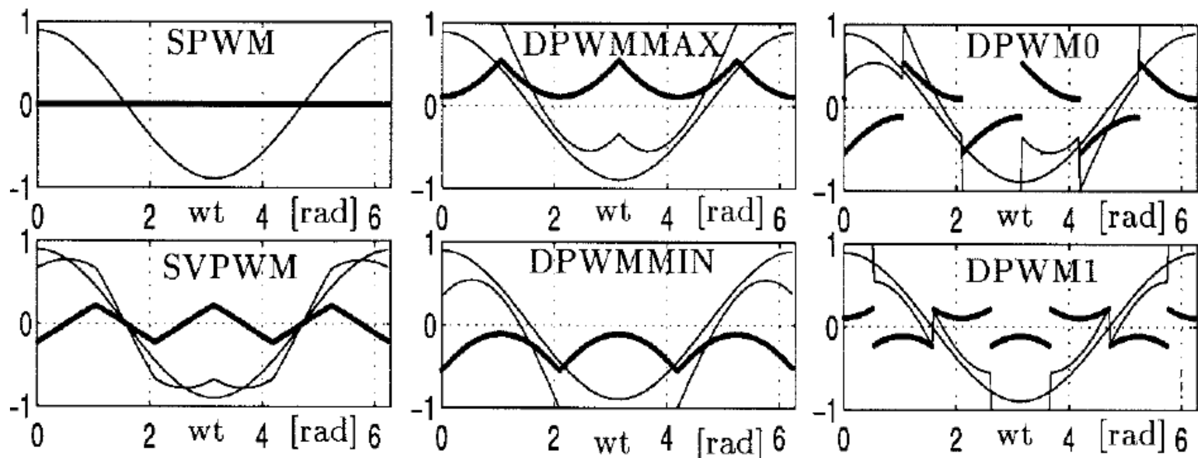

Source: Adapted from Hava, Kerkman and Lipo [1999].

The zero-sequence signal of SVPWM is generated by employing the minimum magnitude test which compares the magnitudes of the three reference signals and selects the signal with minimum magnitude. Scaling this signal by 0.5, the zero-sequence signal of SVPWM is found. Assume $|v_a^*| \leq |v_b^*|, |v_c^*|$, then $v_0 = 0.5v_a^*$

In DPMIN the reference signal with the minimum value defines the zero sequence and in DPMAX is the reference signal with the maximum value. Assume $v_a^* \leq v_b^* \leq v_c^*$, then $v_0 = (V_{dc}/2) - v_c^*$.

DPWM0 and DPWM1 are special cases of a generalized DPWM (GDPWM) method (Hava, Kerkman and Lipo [1998]). Figure 54 illustrates the zero-sequence signal

generation method of GDPWM. The shaded signal is the zero-sequence signal which is equal to the difference between the saturation line ($V_{dc}/2$) and the reference modulation signal which passes the maximum magnitude test. In the maximum magnitude test, all three reference modulation signals v_a^*, v_b^* and v_c^* are phase shifted by $\psi - (\pi/6)$, and of the three new signals $v_{ax}^*, v_{bx}^*, v_{cx}^*$, the one with the maximum magnitude determines the zero-sequence signal. Assume $|v_{ax}^*| \geq |v_{bx}^*|, |v_{cx}^*|$, then $v_0 = (sign(v_a^*))(V_{dc}/2)$. DPWM0 in when $\psi = 0$ and DPWM1 in when $\psi = (\pi/6)$.

Figure 54 – Generating the GDPWM zero-sequence signal with the ψ variable.

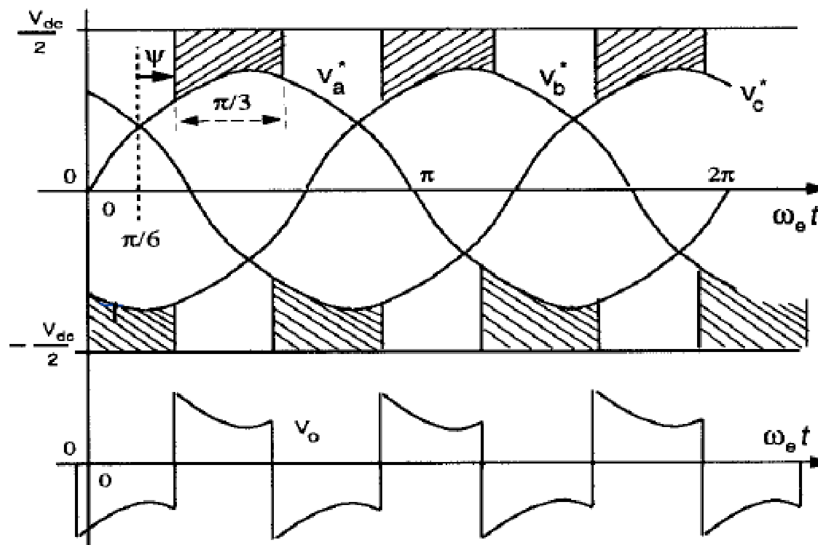

Source: Hava, Kerkman and Lipo [1999].

Table 7 shows the input power, output power and total losses for every test.

Table 7 – Values of input power, output power and total losses for PWM method variation.

PWM Method	P_{in} **(W)**	P_{out} **(W)**	**Losses (W)**
SVPWM	7347	7207	139.90
SPWM	7355	7210	145.26
DPmin	7420	7305	114.56
DPmax	7420	7371	118.83
D0	7466	7348	118.63
D1	7495	7371	124.07

The method that presented the lower losses was the DPMIN. The change in the PWM method also impacts ΔT_j. As shown in Figure 55, there are small temperature variations between each method. The PWM method with the lowest losses also results in the lowest average temperature. With a reduced average temperature, R_{DSon} is lower, which in turn decreases the switching losses. As a result, the temperature variation is also minimized.

Figure 55 – Measured temperature for different PWM methods.

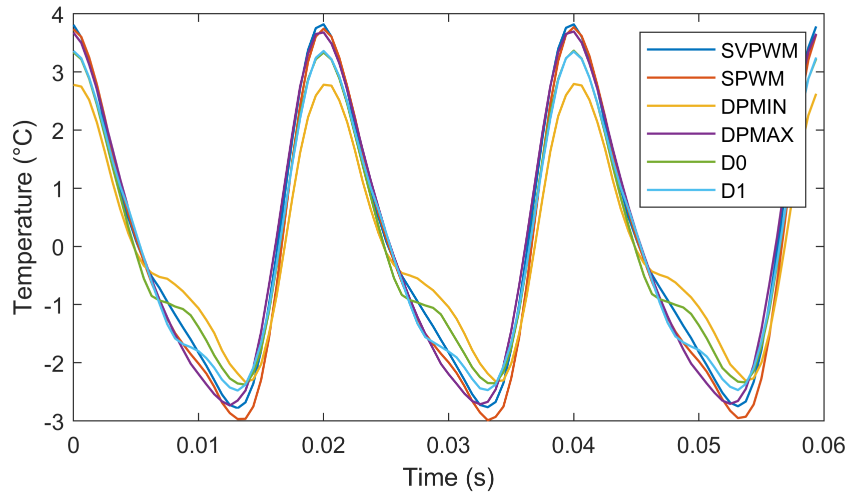

Source: Author.

4.1.4 Fundamental frequency variation

Table 8 shows the input power, output power and total losses for fundamental frequencies of 10Hz, 20Hz, 30Hz, 50Hz, 100Hz and 200Hz. As can be seen, the losses do not significantly change with fundamental frequency. However, as Figure 56 shows, ΔT_j is lower for higher fundamental frequencies. Temperature variation changes from 23°C at 10Hz to 0.9°C at 200Hz.

Table 8 – Values of current, input power, output power and total losses for fundamental frequency variation.

Fundamental Frequency	P_{in} **(W)**	P_{out} **(W)**	**Losses (W)**
10Hz	7738	7587	151.13
20Hz	7680	7530	149.81
30Hz	7592	7443	148.63
50Hz	7341	7191	149.32
100Hz	6377	6228	148.55
200Hz	4010	3949	150.47

As explained in Cougo et al. [2020a], this means that applications having the same fundamental frequency as the one in the existing internal aircraft electrical network (400Hz) or high-speed motor drive applications (higher than 500Hz) present lower ΔT_j, which increases power module lifetime, even if it has more thermal cycles per second. However, in aircraft applications such as inverters for future aircraft internal distribution systems (230V/50Hz) and low-speed motor drives, ΔT_j may be quite high, reducing power module lifetime.

Figure 56 – Measured temperature for fundamental frequencies of 10, 20, 30, 50, 100 and 200Hz (normalized for the 10Hz period).

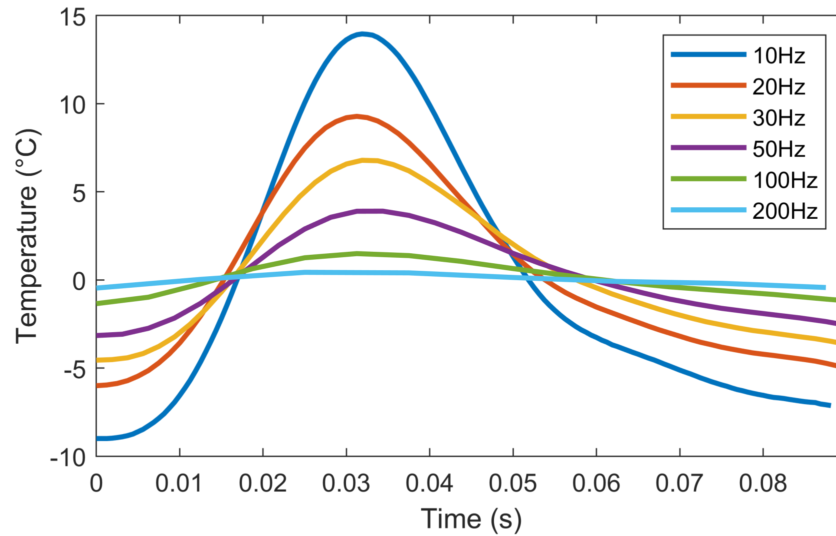

Source: Author.

4.1.5 Switching frequency Variation

As expected, the tests with different switching frequencies shows that losses increases with frequency, as shown in Table 9. Although the measured value at 50 kHz appears to be incorrect due to a measurement error, it was expected that the variation in losses from 30 kHz to 50 kHz would be similar to that observed from 20 kHz to 30 kHz. Also as expected, ΔT_j increases with switching frequency as can be seen in Figure 57.

Table 9 – Values of current, input power, output power and total losses for switching frequency variation (* A higher than expected value, likely caused by a measurement device error).

Switching Frequency	P_{in} **(W)**	P_{out} **(W)**	**Losses (W)**
20kHz	7389	7310	79.22
30kHz	7352	7263	88.86
50kHz	7354	7207	146.71*

Figure 57 – Measured temperature for switching frequencies of 20kHz, 30kHz and 50kHz.

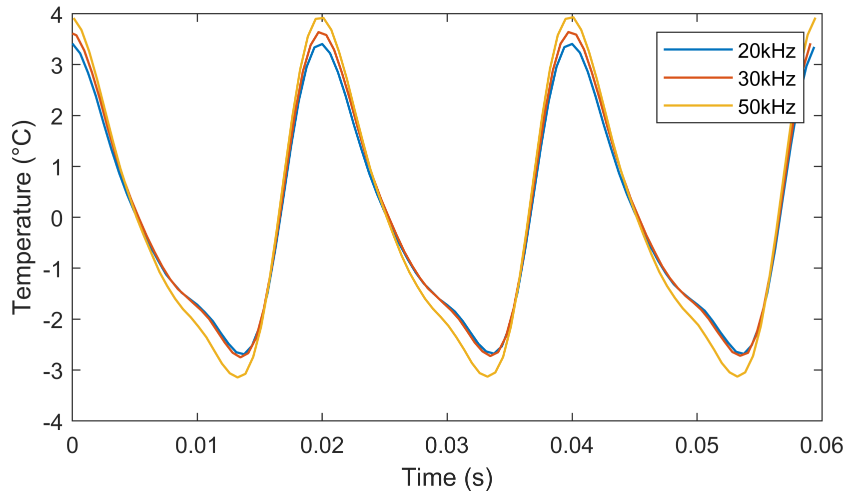

Source: Author.

4.2 Precise Loss Calculation in Three-Phase Converters

An accurate instantaneous loss model, combined with a thermal model, is essential for junction temperature and lifetime estimation of a die. Most of the losses in a three-phase inverter are due to the losses in power transistors, which depend on conduction and switching losses. Accurate models for estimating losses of SiC transistors in three-phase inverters have already been widely studied in Cougo et al. [2020a], and will be briefly presented.

4.2.1 Conduction Losses

Total conduction losses in a switching leg can be simply calculated as

$$P_{cond} = R_{DSon}.{I_{oRMS}}^2 \tag{4.1}$$

where I_{oRMS} is the RMS value of the current in each leg (composed of fundamental value and harmonics) and R_{DSon} is the on-state resistance of a MOSFET for a given junction temperature. An algorithm using MATLAB was created by the authors in Cougo et al. [2020a] to compute conduction losses in the two transistors of one leg of a three-phase inverter. It calculates the conduction losses for each point of the output current within a period of its fundamental frequency. To determine the instantaneous current, it was multiplied by the switching signal. To calculate the instantaneous conduction losses at each point, the value of R_{DSon} needs to be determined. Since V_{gs} is usually fixed when the

transistor is on, and since the junction temperature does not significantly vary during a fundamental period, R_{DSon} must be calculated only for each current I_{DS}. This was done by the use of curves of R_{DSon} vs T_j and R_{DSon} vs I_{DS}, in addition of applying a linear interpolation to find R_{DSon} for a given current I_{DS}, as shown below.

$$R_{DSon}(T_j) = \frac{(T_j - 25°C)}{(150°C - 25°C)}(R_{DSon}(150°C) - R_{DSon}(25°C)) + R_{DSon}(25°C) \quad (4.2)$$

The use of this equation is only possible because the characteristic of this SiC between 25°C and 150°C is almost linear.

4.2.2 Switching Losses

Switching losses are significantly more complicated to estimate, since there is not enough data given by manufacturers or they may not be representative of switching losses in the real converter. It is necessary to determine the switching energies to estimate the losses. The 'double pulse' method is often used in datasheets, but it has some drawbacks, as it requires measuring the current in the component. Therefore, a more accurate method for fast components, called the 'modified opposition method', proposed in Cougo, Schneider and Meynard [2013], is used to characterize the switching energies. The switched current can be determined by using the waveform of the output current, for each duty cycle of a fundamental period. Depending on the direction of the current and the commutation of the output voltage, it can be determined whether turn-off or turn-on energy was dissipated. With this information, the switching energy for each switching event throughout the entire fundamental period can be calculated, allowing for the estimation of switching losses.

4.3 Comparison with thermal model

The estimation of instantaneous junction temperature can be achieved by applying the time signal of the losses in each component to the Foster thermal model of the SiC die. The instantaneous losses in the inverter were calculated using the method mentioned earlier for every combination of parameter variations presented in Section 4.1. The method for calculating the thermal model was detailed in Chapter 3, where it was also demonstrated how the choice of the region of interest for temperature measurement can impact the obtained values. The model was based on the measurement of the average temperature of the SiC die. In this section, a different thermal model is calculated using the temperature measurement from a single point on the metallization surface of the SiC die. The values of thermal resistances and capacitances of this new model are shown in Table 10.

Table 10 – Thermal resistances and capacitances values of the SiC die in a power module, calculated by using temperature measured in a single pixel on the top metallization of the SiC die.

RC elements (i)	Positive current $V_{gs} = 20$V		Negative current $V_{gs} = 20$V	
	R_i (K/W)	C_i (J/K)	R_i (K/W)	C_i (J/K)
1	0.252	1.663	0.384	0.013
2	0.403	0.186	0.199	2.556
3	0.289	0.051	0.410	0.253
4	0.379	0.009	0.040	12.876
5	0.078	0.540	0.333	0.079
6	0.048	5.452	0.077	0.342

The characteristics of the SiC power module used in this work (CPM2–1200-0080B from Cree), such as turn-on and turn-off energies, variation of R_{DSon} with T_j, gate resistance, as well as the operating parameters for each test and the output current information were entered into the MATLAB loss calculation program. The waveforms of instantaneous conduction, switching and total losses in the power module with $f_{fund} =$ 50Hz, $f_{sw} = 50$kHz, $I_{rms} = 14.63$A, $M_i = 0.9$ and SPWM method, for high side (blue line) and low side (red line) transistor in a leg of the inverter are shown in Figure 58.

Figure 58 – Instantaneous (a) conduction,(b) switching and (c) total losses in SiC dies in a switching leg of a three-phase with $f_{fund} = 50$Hz, $f_{sw} = 50$kHz, $M_i = 0.9$ and SPWM method.

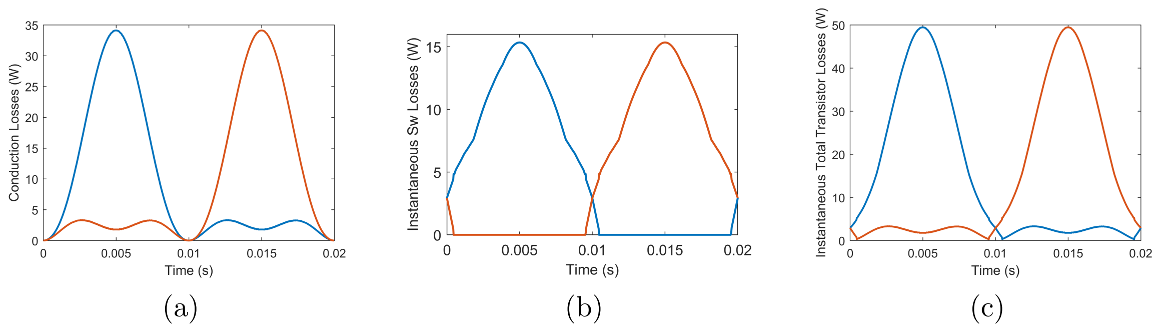

Source: Author

These losses were then applied to the thermal impedance model to estimate the junction temperature. Figure 59 shows the temperature variation in the SiC die measured by the thermal camera and calculated with the thermal model (a) with the average temperature and (b) with the temperature in a single point of the die. Note that on the graph on the left, ΔT_j measured by the camera is equal to 6.3°C and ΔT_j calculated by the model is equal to 5.6°C, hence a difference of 0.7°C (error = 11%). On the graph on the right, ΔT_j measured by the camera is equal to 12.5°C and ΔT_j calculated by the model is equal to 14.4°C, therefore a difference of 1.9°C (error = 15%).

Figure 59 – Junction temperature in SiC die: measured and calculated using the developed thermal model (f_{fund} = 50Hz, f_{sw} = 50kHz, M_i = 0.9 and SPWM method).

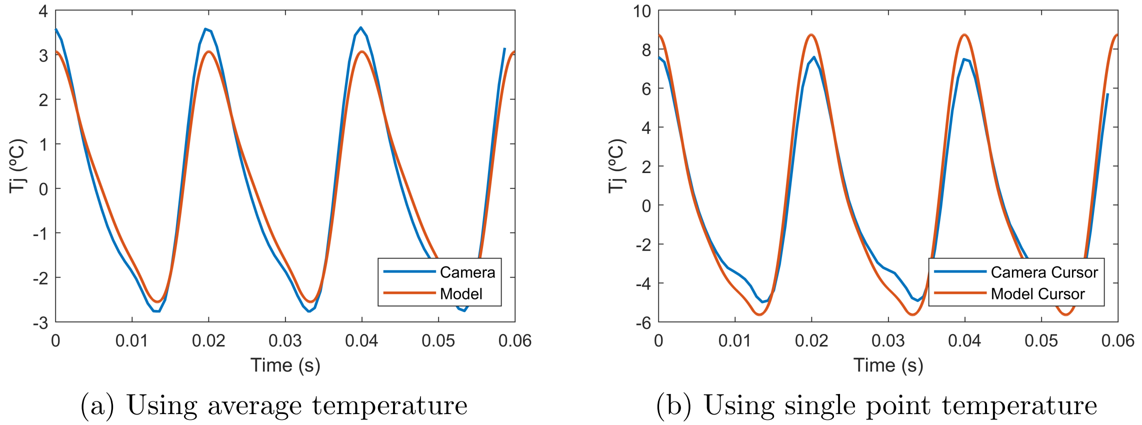

(a) Using average temperature (b) Using single point temperature

Source: Author.

The waveforms of instantaneous conduction, switching and total losses in the power module with f_{fund} = 50Hz, f_{sw} = 50kHz, M_i = 0.357 and SPWM method, for high side (blue line) and low side (red line) transistor in a leg of the inverter are shown in Figure 60. The temperature variation in the SiC die for this operation is shown in Figure 61. On the graph on the left, ΔT_j measured by the camera is equal to 4.6°C and ΔT_j calculated by the model is equal to 4.2°C, hence a difference of 0.4°C (error = 8.7%). On the graph on the right, ΔT_j measured by the camera is equal to 8.7°C and ΔT_j calculated by the model is equal to 10.8°C, therefore a difference of 2.1°C (error = 24%).

Figure 60 – Instantaneous values of (a) conduction,(b) switching and (c) total losses in a three-phase inverter with f_{fund} = 50Hz, f_{sw} = 50kHz and M_i = 0.357 and SPWM method.

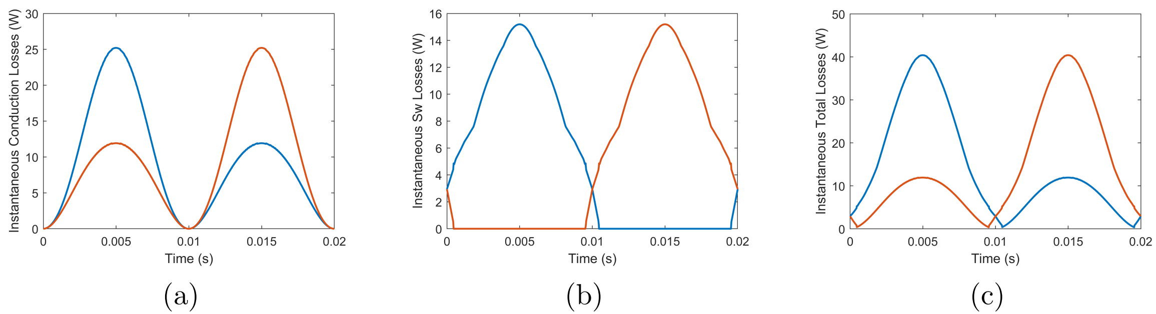

(a) (b) (c)

Source: Author.

These two examples demonstrate that the model using the average temperature slightly underestimates the actual temperature, while the model using the temperature at a single point on the metallization of the die overestimates it. However, both models are effective in accurately estimating the junction temperature of the SiC die. Another

Figure 61 – Junction temperature in SiC die: measured and calculated by thermal model using (a) average temperature and (b) single point temperature (f_{fund} = 50Hz, f_{sw} = 50kHz and M_i = 0.357 and SPWM method).

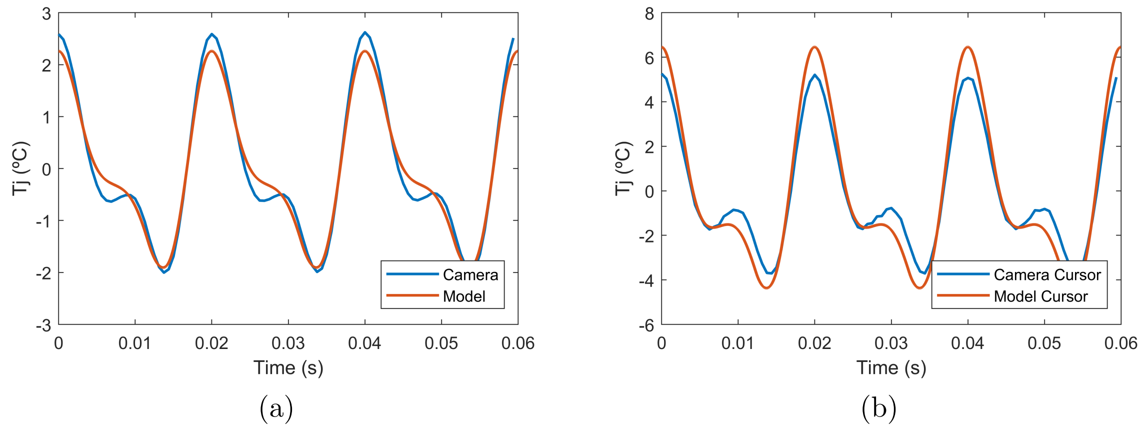

Source: Author.

interesting result is shown in Figure 62 for f_{fund} = 50Hz, f_{sw} = 50kHz, M_i = 0.9, I = 21.11Arms and SPWM method. In this situation the temperature measured by the thermal camera is ΔT_j = 25.2°C. This amplitude value is very significant and was never experimentally shown in the literature for such a fast (50Hz) thermal cycle. Using the classical lifetime modeling with this data, it apparently sub-estimates the number of cycles before failure in the SiC MOSFET.

Figure 62 – Junction temperature in SiC die: measured and calculated by thermal model using single point method (f_{fund} = 50Hz, f_{sw} = 50kHz and M_i = 0.357, I = 21.11Arms and SPWM method).

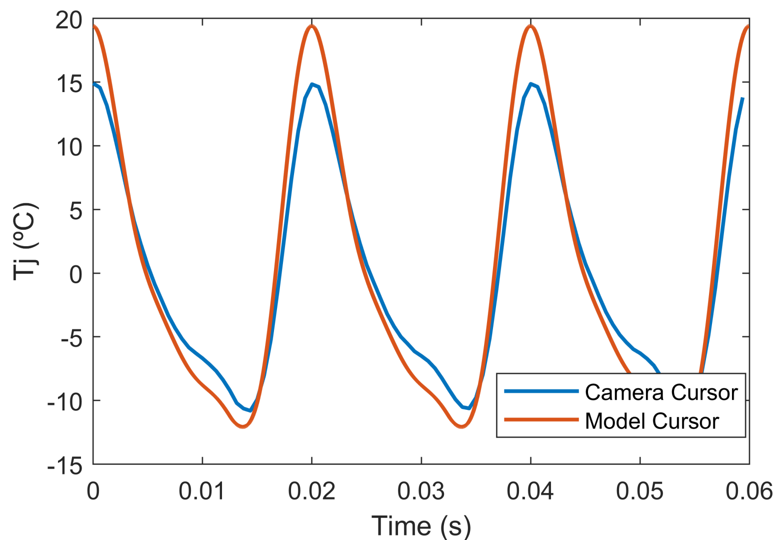

Source: Author.

4.4 Chapter overview

This chapter presented results of temperature measurements in a real three-phase inverter operating at different switching frequencies, output currents, fundamental frequencies, PWM methods and modulation indexes. It was also showed the comparison between the measured temperature and the temperature calculated by two thermal impedance model, one made with the average temperature of he SiC the and the other with the temperature of a single pixel in the die. Results shows that the model estimates the junction temperature with accuracy and could be used for lifetime reliability studies.

Chapter 5

Conclusion

High-performance three-phase inverters are now commonly built using SiC transistors. These components are known for their low power losses, but they also have low thermal capacitance, which leads to significant temperature fluctuations during the fundamental period of the inverter's output current. Although these temperature changes are relatively small (a few degrees Celsius or even fractions of a degree), they occur very frequently (at tens of Hertz), potentially shortening the lifespan of a power module that includes these SiC transistors. This thesis presented a method for creating an accurate SiC component thermal model and measurement of junction temperature in a real three-phase inverter.

Chapter 2 provided a literature review on the reliability of SiC devices and on temperature measurement methods for semiconductor devices. Unlike silicon, which has well-established studies, SiC devices are still relatively new to the market and require further research to achieve a deeper understanding of their reliability. Some failure mechanisms of SiC MOSFETs were discussed, such as gate threshold voltage degradation, body diode degradation, avalanche events, degradation in gate leakage current and degradation under power cycling stress. Lifetime models are important tools in the field of reliability, as they allow for the calculation of power cycling expectations. The most widely used models were created based on IGBT components, however, it is known that they do not provide accurate estimation for low thermal cycles in SiC MOSFETs. New studies are evaluating reliability within this temperature range, making the measurement and estimation of junction temperature in these components crucial.

Chapter 3 presents a method for accurately estimating temperature variation of SiC dies used in three-phase inverters, with the aim of estimating component lifetime. The method is based on temperature measured with fast and accurate infrared thermal camera, for different current direction through the SiC die. It was found that the thermal impedance of the die does not significantly vary with its losses, but it does vary by 10–20% with respect to the current direction inside the die. The model developed was partially

validated with sinusoidal current on the SiC die. It was observed that there is a significant temperature variation of these SiC dies having current flowing at frequencies corresponding to those in three-phase converters (some tens of Hertz). This temperature variation can significantly reduce lifetime of SiC-based modules.

Chapter 4 shows measured temperature variation on the metallization of 'Source' terminal of SiC dies inside a power module used in a three-phase inverter for aircraft applications, providing power to a RL load emulating an electrical actuator. In this setup, different parameters such as switching frequencies, current amplitude and fundamental frequencies, modulation indexes and DC bus voltage could easily be changed. A measurement of the SiC die has a thermal cycle amplitude of 25°C, a value that is very significant and was never experimentally shown in the literature for such a fast (50Hz) thermal cycle. The measured temperatures were compared with the temperature calculated by the thermal impedance model and was confirmed that the model can accurately estimate the temperature and can be used for reliability studies.

5.1 Future Works

The work presented brings relevant results for understanding low thermal cycles in SiC MOSFETs, which can influence their reliability. A proposal for continuation would be to understand "if and how" such fast thermal cycles can be dangerous and significantly reduce SiC power modules lifetime. Besides performing power cycle tests to evaluate SiC component lifetime, one of the most important results is to develop the technique and test bench to apply power cycle at high frequency (10 to 100Hz). However, the greatest challenge is to measure junction temperature variation at this frequency (by optical or infrared means), or to guarantee that indirect temperature measurement (by voltage drop or RDSon measurement) give trustable results.

References

ABSTREITER, G. Micro-raman spectroscopy for characterization of semiconductor devices. *Applied Surface Science*, v. 50, n. 1, p. 73–78, 1991. ISSN 0169-4332. ⟨https://doi.org/10.1016/0169-4332(91)90141-6⟩.

ALDéN, M. et al. Thermographic phosphors for thermometry: A survey of combustion applications. *Progress in Energy and Combustion Science*, v. 37, n. 4, p. 422–461, 2011. ISSN 0360-1285. ⟨https://doi.org/10.1016/j.pecs.2010.07.001⟩.

AVENAS, Y.; DUPONT, L.; KHATIR, Z. Temperature measurement of power semiconductor devices by thermo-sensitive electrical parameters—a review. *IEEE Transactions on Power Electronics*, v. 27, n. 6, p. 3081–3092, 2012. ⟨http://dx.doi.org/10.1109/TPEL.2011.2178433⟩.

AZAR, K.; FARINA, D. Measuring chip temperature with thermochromic liquid crystals. *Electronics Cooling*, FLOMERICS LIMITED, v. 3, p. 16–22, 1997.

BAKER, N. et al. Ir camera validation of igbt junction temperature measurement via peak gate current. *IEEE Transactions on Power Electronics*, v. 32, n. 4, p. 3099–3111, 2017. ⟨http://dx.doi.org/10.1109/TPEL.2016.2573761⟩.

BATUNLU, C.; ALBARBAR, A. A technique for mitigating thermal stress and extending life cycle of power electronic converters used for wind turbines. *Electronics*, v. 4, n. 4, p. 947–968, 2015. ISSN 2079-9292. ⟨http://dx.doi.org/10.3390/electronics4040947⟩.

BAYERER, R. et al. Model for power cycling lifetime of igbt modules - various factors influencing lifetime. In: *5th International Conference on Integrated Power Electronics Systems*. [S.l.: s.n.], 2008. p. 1–6.

BLACKBURN, D. Temperature measurements of semiconductor devices - a review. In: *Twentieth Annual IEEE Semiconductor Thermal Measurement and Management Symposium (IEEE Cat. No.04CH37545)*. [s.n.], 2004. p. 70–80. ⟨http://dx.doi.org/10.1109/STHERM.2004.1291304⟩.

CAHILL, D. G.; GOODSON, K.; MAJUMDAR, A. Thermometry and Thermal Transport in Micro/Nanoscale Solid-State Devices and Structures . *Journal of Heat Transfer*, v. 124, n. 2, p. 223–241, 12 2001. ISSN 0022-1481. ⟨http://dx.doi.org/10.1115/1.1454111⟩.

CHEN, H. et al. On-line monitoring of the mosfet device junction temperature by computation of the threshold voltage. In: *2006 3rd IET International Conference on Power Electronics, Machines and Drives - PEMD 2006*. [S.l.: s.n.], 2006. p. 440–444.

COUGO, B. et al. Influence of pwm methods on semiconductor losses and thermal cycling of 15-kva three-phase sic inverter for aircraft applications. *Electronics*, v. 9, n. 4, 2020. ISSN 2079-9292. ⟨http://dx.doi.org/10.3390/electronics9040620⟩.

COUGO, B. et al. Characterization of low-inductance sic module with integrated capacitors for aircraft applications requiring low losses and low emi issues. *IEEE Transactions on Power Electronics*, IEEE, v. 36, n. 7, p. 8230–8242, 2020. ⟨http://dx.doi.org/10.1109/TPEL.2020.3014529⟩.

COUGO, B.; SCHNEIDER, H.; MEYNARD, T. Accurate switching energy estimation of wide bandgap devices used in converters for aircraft applications. In: *2013 15th European Conference on Power Electronics and Applications (EPE)*. [s.n.], 2013. p. 1–10. ⟨http://dx.doi.org/10.1109/EPE.2013.6634338⟩.

DASGUPTA, S. et al. Analysis and prediction of stability in commercial, 1200 v, 33a, 4h-sic mosfets. In: *2012 IEEE International Reliability Physics Symposium (IRPS)*. [s.n.], 2012. p. 3D.3.1–3D.3.5. ⟨http://dx.doi.org/10.1109/IRPS.2012.6241817⟩.

DUPONT, L.; AVENAS, Y.; JEANNIN, P.-O. Comparison of junction temperature evaluations in a power igbt module using an ir camera and three thermosensitive electrical parameters. *IEEE Transactions on Industry Applications*, v. 49, n. 4, p. 1599–1608, 2013. ⟨http://dx.doi.org/10.1109/TIA.2013.2255852⟩.

DUPONT, L. et al. Accelerated active ageing test on sic jfets power module with silver joining technology for high temperature application. *Microelectronics Reliability*, v. 49, n. 9, p. 1375–1380, 2009. ISSN 0026-2714. 20th European Symposium on the Reliability of Electron Devices, Failure Physics and Analysis. ⟨https://doi.org/10.1016/j.microrel.2009.07.050⟩.

DZIARSKI, K. et al. Methods of measurement of die temperature of semiconductor elements: A review. *Energies*, v. 16, n. 6, 2023. ISSN 1996-1073. ⟨http://dx.doi.org/10.3390/en16062559⟩.

FALCK, J. et al. Reliability of power electronic systems: An industry perspective. *IEEE Industrial Electronics Magazine*, v. 12, n. 2, p. 24–35, 2018. ⟨http://dx.doi.org/10.1109/MIE.2018.2825481⟩.

FAYYAZ, A.; ROMANO, G.; CASTELLAZZI, A. Body diode reliability investigation of sic power mosfets. *Microelectronics Reliability*, v. 64, p. 530–534, 2016. ISSN 0026-2714. Proceedings of the 27th European Symposium on Reliability of Electron Devices, Failure Physics and Analysis. ⟨https://doi.org/10.1016/j.microrel.2016.07.044⟩.

FIRST Commercial Silicon Carbide Power MOSFET. 2011. ⟨https://eeweb.com/first-commercial-silicon-carbide-power-mosfet/⟩. Accessed on: July 25, 2024.

FLIR. Research ir user's guide. 2016.

GONZALEZ, J. O. et al. An investigation of temperature-sensitive electrical parameters for sic power mosfets. *IEEE Transactions on Power Electronics*, v. 32, n. 10, p. 7954–7966, 2017. ⟨http://dx.doi.org/10.1109/TPEL.2016.2631447⟩.

GOPIREDDY, L. R.; TOLBERT, L. M.; OZPINECI, B. Power cycle testing of power switches: A literature survey. *IEEE Transactions on Power Electronics*, v. 30, n. 5, p. 2465–2473, 2015. ⟨https://doi.org/10.1109/TPEL.2014.2359015⟩.

GRIFFO, A. et al. Real-time measurement of temperature sensitive electrical parameters in sic power mosfets. *IEEE Transactions on Industrial Electronics*, v. 65, n. 3, p. 2663–2671, 2018. ⟨http://dx.doi.org/10.1109/TIE.2017.2739687⟩.

HAVA, A.; KERKMAN, R.; LIPO, T. A high-performance generalized discontinuous pwm algorithm. *IEEE Electronic Library (IEL) Journals*, v. 34, n. 5, p. 1059–1071, 1998. ⟨http://dx.doi.org/10.1109/28.720446⟩.

HAVA, A.; KERKMAN, R.; LIPO, T. Simple analytical and graphical methods for carrier-based pwm-vsi drives. *IEEE Transactions on Power Electronics*, v. 14, n. 1, p. 49–61, 1999. ⟨http://dx.doi.org/10.1109/63.737592⟩.

HOFFMANN, F.; KAMINSKI, N.; SCHMITT, S. Comparison of the power cycling performance of silicon and silicon carbide power devices in a baseplate less module package at different temperature swings. In: *2021 33rd International Symposium on Power Semiconductor Devices and ICs (ISPSD)*. [s.n.], 2021. p. 175–178. ⟨http://dx.doi.org/10.23919/ISPSD50666.2021.9452242⟩.

HOFFMANN, F.; SCHMITT, S.; KAMINSKI, N. Lifetime modeling of sic mosfet power modules during power cycling tests at low temperature swings. In: *2023 35th International Symposium on Power Semiconductor Devices and ICs (ISPSD)*. [s.n.], 2023. p. 294–297. ⟨http://dx.doi.org/10.1109/ISPSD57135.2023.10147533⟩.

HU, B. et al. Failure and reliability analysis of a sic power module based on stress comparison to a si device. *IEEE Transactions on Device and Materials Reliability*, v. 17, n. 4, p. 727–737, 2017. ⟨http://dx.doi.org/10.1109/TDMR.2017.2766692⟩.

JEON, J. G. et al. High-precision ionic thermocouples fabricated using potassium ferri/ferrocyanide and iron perchlorate. *Advanced Electronic Materials*, v. 8, n. 5, p. 2100693, 2022. ⟨https://doi.org/10.1002/aelm.202100693⟩.

KAPLAR, R. et al. Characterization and reliability of sic-and gan-based power transistors for renewable energy applications. In: IEEE. *2012 IEEE Energytech*. 2012. p. 1–6. ⟨https://doi.org/10.1109/EnergyTech.2012.6304627⟩.

KENDIG, D. et al. Side-by-side comparison between infrared and thermoreflectance imaging using a thermal test chip with embedded diode temperature sensors. In: *2012 28th Annual IEEE Semiconductor Thermal Measurement and Management Symposium (SEMI-THERM)*. [s.n.], 2012. p. 344–347. ⟨http://dx.doi.org/10.1109/STHERM.2012.6188871⟩.

KHATIR, Z. Junction temperature investigations based on a general semi-analytical formulation of forward voltage of power diodes. *IEEE Transactions on Electron Devices*, v. 59, n. 6, p. 1716–1722, 2012. ⟨http://dx.doi.org/10.1109/TED.2012.2190515⟩.

KOENIG, A. et al. On-line junction temperature measurement of coolmos devices. In: *2007 7th International Conference on Power Electronics and Drive Systems*. [s.n.], 2007. p. 90–95. ⟨http://dx.doi.org/10.1109/PEDS.2007.4487683⟩.

KOVACEVIC-BADSTUEBNER, I. et al. Power cycling reliability of sic mosfets in discrete and module packages. In: *2022 IEEE International Reliability Physics Symposium (IRPS)*. [s.n.], 2022. p. 10C.3–1–10C.3–6. ⟨http://dx.doi.org/10.1109/IRPS48227.2022.9764498⟩.

KOZAK, J. P. et al. Impact of accelerated stress-tests on sic mosfet precursor parameters. In: *2018 Second International Symposium on 3D Power Electronics Integration and Manufacturing (3D-PEIM)*. [s.n.], 2018. p. 1–5. ⟨http://dx.doi.org/10.1109/3DPEIM.2018.8525234⟩.

KUBALL, M. et al. Time-resolved temperature measurement of algan/gan electronic devices using micro-raman spectroscopy. *IEEE Electron Device Letters*, v. 28, n. 2, p. 86–89, 2007. ⟨http://dx.doi.org/10.1109/LED.2006.889215⟩.

KUHN, H.; MERTENS, A. On-line junction temperature measurement of igbts based on temperature sensitive electrical parameters. In: *2009 13th European Conference on Power Electronics and Applications*. [S.l.: s.n.], 2009. p. 1–10.

LI, C. et al. Online junction temperature extraction of sic power mosfets with temperature sensitive optic parameter (tsop) approach. *IEEE Transactions on Power Electronics*, v. 34, n. 10, p. 10143–10152, 2019. ⟨http://dx.doi.org/10.1109/TPEL.2018.2890303⟩.

LUTZ, J. et al. Validity of power cycling lifetime models for modules and extension to low temperature swings. In: *2020 22nd European Conference on Power Electronics and Applications (EPE'20 ECCE Europe)*. [s.n.], 2020. p. P.1–P.9. ⟨http://dx.doi.org/10.23919/EPE20ECCEEurope43536.2020.9215609⟩.

MA, K. et al. Thermal loading and lifetime estimation for power device considering mission profiles in wind power converter. *IEEE Transactions on Power Electronics*, v. 30, n. 2, p. 590–602, 2015. ⟨http://dx.doi.org/10.1109/TPEL.2014.2312335⟩.

MASSON, A. et al. High-temperature die-attaches for sic power devices. In: IEEE. *Proceedings of the 2011 14th European Conference on Power Electronics and Applications*. [S.l.], 2011. p. 1–10.

MATEI, C. et al. Dynamic temperature measurements of a gan dc–dc boost converter at mhz frequencies. *IEEE Transactions on Power Electronics*, v. 35, n. 8, p. 8303–8310, 2020. ⟨http://dx.doi.org/10.1109/TPEL.2020.2964996⟩.

NEL, B.; PERINPANAYAGAM, S. A brief overview of sic mosfet failure modes and design reliability. *Procedia CIRP*, v. 59, p. 280–285, 2017. ISSN 2212-8271. Proceedings of the 5th International Conference in Through-life Engineering Services Cranfield University, 1st and 2nd November 2016. ⟨http://dx.doi.org/https://doi.org/10.1016/j.procir.2016.09.025⟩.

NGUYEN, Q. C. *Développement d'outils électrothermiques pour la localisation de défauts et pour l'optimisation de la performance de modules mécatroniques de puissance SiC*. PhD (Dissertation) — INSA de Toulouse, 2021.

NGUYEN, T.-T. et al. Gate oxide reliability issues of sic mosfets under short-circuit operation. *IEEE Transactions on Power Electronics*, v. 30, n. 5, p. 2445–2455, 2015. ⟨https://doi.org/10.1109/TPEL.2014.2353417⟩.

NGWASHI, D. K.; PHUNG, L. V. Recent review on failures in silicon carbide power mosfets. *Microelectronics Reliability*, v. 123, p. 114169, 2021. ISSN 0026-2714. ⟨https://doi.org/10.1016/j.microrel.2021.114169⟩.

NOWAK, M.; RABKOWSKI, J.; BARLIK, R. Measurement of temperature sensitive parameter characteristics of semiconductor silicon and silicon -carbide power devices. In: *2008 13th International Power Electronics and Motion Control Conference*. [s.n.], 2008. p. 84–87. ⟨http://dx.doi.org/10.1109/EPEPEMC.2008.4635248⟩.

OSTERMEIR, R. et al. Temperature distribution in si-mosfets studied by micro-raman spectroscopy. *IEEE Transactions on Electron Devices*, v. 39, n. 4, p. 858–863, 1992. ⟨10.1109/16.127476⟩.

PARK, J.; SHIN, M. W.; LEE, C. Thermal modeling and measurement of gan-based hfet devices. *IEEE Electron Device Letters*, v. 24, n. 7, p. 424–426, 2003. ⟨http://dx.doi.org/10.1109/LED.2003.814020⟩.

POPOV, V. M. et al. Liquid-crystal thermography of hot spots on electronic components. *Russian Microelectronics*, v. 36, p. 392–401, 2007. ⟨https://doi.org/10.1134/S1063739707060066⟩.

REN, N. et al. Investigation on single pulse avalanche failure of sic mosfet and si igbt. *Solid-State Electronics*, v. 152, p. 33–40, 2019. ISSN 0038-1101. ⟨https://doi.org/10.1016/j.sse.2018.11.010⟩.

ROMANO, G. et al. An ultrafast ir thermography system for transient temperature detection on electronic devices. In: *2014 Semiconductor Thermal Measurement and Management Symposium (SEMI-THERM)*. [s.n.], 2014. p. 80–84. ⟨http://dx.doi.org/10.1109/SEMI-THERM.2014.6892219⟩.

RUTHARDT, J. et al. Lifetime extension of power semiconductor devices by closed-loop junction temperature control. In: *2021 23rd European Conference on Power Electronics and Applications (EPE'21 ECCE Europe)*. [s.n.], 2021. p. 1–10. ⟨http://dx.doi.org/10.23919/EPE21ECCEEurope50061.2021.9570681⟩.

SCHEUERMANN, U.; JUNGHAENEL, M. Limitation of power module lifetime derived from active power cycling tests. In: *CIPS 2018; 10th International Conference on Integrated Power Electronics Systems*. [S.l.: s.n.], 2018. p. 1–10.

SCHEUERMANN, U.; SCHMIDT, R.; NEWMAN, P. Power cycling testing with different load pulse durations. In: *7th IET International Conference on Power Electronics, Machines and Drives (PEMD 2014)*. [s.n.], 2014. p. 1–6. ⟨http://dx.doi.org/10.1049/cp.2014.0475⟩.

SCHROCK, J. A. et al. High-mobility stable 1200-v, 150-a 4h-sic dmosfet long-term reliability analysis under high current density transient conditions. *IEEE Transactions on Power Electronics*, v. 30, n. 6, p. 2891–2895, 2015. ⟨http://dx.doi.org/10.1109/TPEL.2014.2357013⟩.

SHARMA, K. et al. A robust approach for characterization of junction temperature of sic power devices via quasi-threshold voltage as temperature sensitive electrical parameter. In: *2020 IEEE Applied Power Electronics Conference and Exposition (APEC)*. [s.n.], 2020. p. 1532–1536. ⟨http://dx.doi.org/10.1109/APEC39645.2020.9124609⟩.

SMET, V. et al. Ageing and failure modes of igbt modules in high-temperature power cycling. *IEEE Transactions on Industrial Electronics*, v. 58, n. 10, p. 4931–4941, 2011. ⟨http://dx.doi.org/10.1109/TIE.2011.2114313⟩.

STELLA, F. et al. Online junction temperature estimation of sic power mosfets through on-state voltage mapping. *IEEE Transactions on Industry Applications*, v. 54, n. 4, p. 3453–3462, 2018. ⟨http://dx.doi.org/10.1109/TIA.2018.2812710⟩.

TESTA, A. et al. Stress analysis and lifetime estimation on power mosfets for automotive abs systems. In: *2008 IEEE Power Electronics Specialists Conference*. [s.n.], 2008. p. 1169–1175. ⟨https://doi.org/10.1109/PESC.2008.4592088⟩.

UCHIDA, T.; SUGIE, R. Evaluation of thermal cycle stress in sic power devices by raman spectroscopy. In: *2018 International Conference on Electronics Packaging and iMAPS All Asia Conference (ICEP-IAAC)*. [s.n.], 2018. p. 579–582. ⟨http://dx.doi.org/10.23919/ICEP.2018.8374656⟩.

UEDA, T. Reliability issues in gan and sic power devices. In: *2014 IEEE International Reliability Physics Symposium*. [s.n.], 2014. p. 3D.4.1–3D.4.6. ⟨https://doi.org/10.1109/IRPS.2014.6860629⟩.

UGUR, E.; AKIN, B. Aging assessment of discrete sic mosfets under high temperature cycling tests. In: *2017 IEEE Energy Conversion Congress and Exposition (ECCE)*. [s.n.], 2017. p. 3496–3501. ⟨http://dx.doi.org/10.1109/ECCE.2017.8096624⟩.

VALENTINE, N. et al. Failure Analyses of Modern Power Semiconductor Switching Devices. *IMAPSource Proceedings*, IMAPS, v. 2015, n. 1, p. 690–695, oct 1 2015. ⟨https://doi.org/10.4071/isom-2015-THA56⟩.

WANG, D. et al. Thermal analysis of high-power light-emitting diode using thermoreflectance thermography. In: *2021 22nd International Conference on Electronic Packaging Technology (ICEPT)*. [s.n.], 2021. p. 1–4. ⟨http://dx.doi.org/10.1109/ICEPT52650.2021.9568025⟩.

WANG, J.; JIANG, X. Review and analysis of sic mosfets' ruggedness and reliability. *IET Power Electronics*, v. 13, n. 3, p. 445–455, 2020. ⟨https://doi.org/10.1049/iet-pel.2019.0587⟩.

WANG, R. et al. Sic device junction temperature online monitoring. In: *2018 IEEE Energy Conversion Congress and Exposition (ECCE)*. [s.n.], 2018. p. 387–392. ⟨http://dx.doi.org/10.1109/ECCE.2018.8558298⟩.

YANG, E. et al. Temperature dependence of current gain of gainp/gaas heterojunction and heterostructure-emitter bipolar transistors. *IEEE Transactions on Electron Devices*, v. 46, n. 2, p. 320–323, 1999. ⟨http://dx.doi.org/10.1109/16.740896⟩.

YANG, S. et al. An industry-based survey of reliability in power electronic converters. In: *2009 IEEE Energy Conversion Congress and Exposition*. [s.n.], 2009. p. 3151–3157. ⟨http://dx.doi.org/10.1109/ECCE.2009.5316356⟩.

ZHANG, Y. et al. Impact of lifetime model selections on the reliability prediction of igbt modules in modular multilevel converters. In: *2017 IEEE Energy Conversion Congress and Exposition (ECCE)*. [s.n.], 2017. p. 4202–4207. ⟨http://dx.doi.org/10.1109/ECCE.2017.8096728⟩.

ZHANG, Y. et al. Mission profile-based system-level reliability prediction method for modular multilevel converters. *IEEE Transactions on Power Electronics*, v. 35, n. 7, p. 6916–6930, 2020. ⟨http://dx.doi.org/10.1109/TPEL.2019.2957826⟩.

ZVEREV, I. et al. Sic schottky rectifiers: performance, reliability and key applications. In: *Proceedings of EPE 2001 Conference*. [S.l.: s.n.], 2001.

ŁUKASIAK, L.; JAKUBOWSKI, A. History of semiconductors. *Journal of Telecommunications and Information Technology*, n. 1, p. 3–9, Mar. 2010. ⟨https://doi.org/10.26636/jtit.2010.1.1015⟩.